Formation of long-lived dark states during electronic relaxation of pyrimidine nucleobases studied using extreme ultraviolet time-resolved photoelectron spectroscopy

Yuta Miura,[1,⊥] Yo-ichi Yamamoto,[1] Shutaro Karashima,[1] Natsumi Orimo,[1] Ayano Hara,[1,†] Kanae Fukuoka,[1,‡] Tatsuya Ishiyama,[2] and Toshinori Suzuki[1,*]

[1]*Department of Chemistry, Graduate School of Science, Kyoto University, Kitashirakawa-Oiwakecho, Sakyo-Ku, Kyoto 606-8502, JAPAN*

[2]*Department of Applied Chemistry, Graduate School of Science and Engineering, University of Toyama, Toyama 930-8555, Japan*

Abstract

Ultrafast electronic relaxation of nucleobases from $^1\pi\pi^*$ states to the ground state (S_0) is considered essential for the photostability of DNA. However, transient absorption spectroscopy (TAS) has indicated that some nucleobases in aqueous solutions create long-lived $^1n\pi^*/^3\pi\pi^*$ dark states from the $^1\pi\pi^*$ states with a high quantum yield of 0.4-0.5. We investigated electronic relaxation in pyrimidine nucleobases in both aqueous solutions and the gas phase using extreme ultraviolet (EUV) time-resolved photoelectron spectroscopy. Femtosecond EUV probe pulses cause ionization from all electronic states involved in the relaxation process, providing a clear overview of the electronic dynamics. The $^1n\pi^*$ quantum yields for aqueous cytidine and uracil (Ura) derivatives were found to be considerably lower (<0.07) than previous estimates reported by TAS. On the other hand, aqueous thymine (Thy) and thymidine exhibited a longer $^1\pi\pi^*$ lifetime and a higher quantum yield (0.12-0.22) for $^1n\pi^*$ state. A similar trend was found for isolated Thy and Ura in the gas phase: the $^1\pi\pi^*$ lifetimes are 39 and 17 fs and the quantum yield for $^1n\pi^*$ are 1.0 and 0.45 for Thy and Ura, respectively. The result indicates that single methylation to the C_5 position hinders the out-of-plane deformation that drives the system to the conical intersection region between $^1\pi\pi^*$ and S_0, providing a large impact on the photophysics/photochemistry of a pyrimidine nucleobase. The significant reduction of $^1n\pi^*$ yield in aqueous solution is ascribed to the destabilization of the $^1n\pi^*$ state induced by hydrogen bonding.

TOC graphics

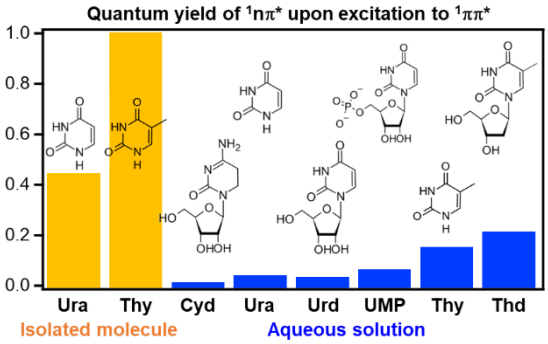

Introduction

Why nucleobases have been chosen to record genetic information is an intriguing scientific question. Nucleobases are known to undergo an ultrafast electronic relaxation process from optically bright $^1\pi\pi^*$ states to the ground electronic state (S_0), which facilitates rapid transformation of absorbed ultraviolet (UV) photon energy into heat, and its rapid dissipation into the surroundings.[1-8] Some researchers have speculated that this mechanism offered advantages for protecting genetic code from photolesion under strong solar radiation through the primitive atmosphere of the early Earth, providing a selection pressure to choose these molecules as the key constituents of DNA/RNA.[9-10]

However, transient absorption spectroscopy (TAS) measurements by Hare et al. indicated that aqueous nucleobases also deactivate from $^1\pi\pi^*$ via long-lived optically dark $^1n\pi^*$ states, and that this relaxation channel has a rather high quantum yield (>0.4) in some pyrimidine nucleobases.[6] This finding seems in contradiction with the conventional picture of the photostability of nucleobases. On the other hand, ultraviolet time-resolved photoelectron spectroscopy (UV-TRPES) studies of aqueous solutions of Thymine (Thy) and Thymidine (Thd) performed by Buchner and coworkers indicated no photoionization signal from $^1n\pi^*$, and they concluded that $^1n\pi^*$ is not involved in the relaxation process from $^1\pi\pi^*$.[11-12] A similar contradiction has been seen between TAS and UV-TRPES results reported by other groups.[13-15] These results suggest that there are fundamental problems in either TAS or UV-TRPES or both in estimation of the quantum yields for the optically dark states.

In the present study, we investigate the photophysics of nucleobases in aqueous solutions using extreme-ultraviolet time-resolved photoelectron spectroscopy (EUV-TRPES). The study on the relaxation dynamics of aqueous nucleobases also provides valuable insights into those of nucleobase pairs in DNA .[14, 16-17] Since the vertical ionization energies from the $^1n\pi^*$ states of aqueous nucleobases are unknown, it is crucial to employ EUV probe pulses (> 20 eV) that ensure ionization from all electronic states involved in the relaxation process, eliminating any ambiguity as to whether or not the probe photon energy was sufficient for ionization from the $^1n\pi^*$ states. The main targets of the present study were cytidine (Cyd), uracil (Ura) and uridine 5'-monophophate (UMP) for which high $^1n\pi^*$ quantum yields of 0.49, 0.28 and 0.42 have been reported, respectively.[6, 14] Uridine (Urd),[18] Thy, and Thd, with slightly smaller estimated values (<0.2), were also studied. The chemical structures of these molecules are depicted in Figure 1.

Since the photophysics of nucleobases is strongly influenced by hydrogen bonding, it is important to compare the dynamics of aqueous nucleobases with those of isolated molecules in the gas phase. However, since nucleosides and nucleotides are vulnerable to evaporation at high temperature,[19-20] we studied gaseous Thy and Ura alternatively.[9, 16, 21-27] Thy and Ura are known to have keto forms in the gas phase almost exclusively; the minute amount of keto-enol tautomers,[28] which have higher energy than the keto form by more than 9 kcal/mol, is practically negligible. On the other hand, the dominant tautomer of gaseous cytosine (Cyt) has a non-canonical form, so that Cyt was excluded in the present study. Early experimental and theoretical studies indicated that $^1\pi\pi^* \rightarrow {}^1n\pi^*$ internal conversion in isolated pyrimidine bases takes several hundred femtoseconds; however, recent studies suggest that the

actual lifetime of $^1\pi\pi^*$ is shorter than 50 fs.[25-27] Thus, we performed EUV-TRPES with a temporal resolution of 47±3 fs to precisely determine the rate and quantum yield for $^1\pi\pi^* \rightarrow {}^1n\pi^*$ internal conversion in isolated molecules.

In the following, we refer to the electronic states relevant to the dynamics as $^1\pi\pi^*$, $^1n\pi^*$, $^3\pi\pi^*$, $^3n\pi^*$ and S_0, which correspond to the diabatic bases most typically employed in spectroscopic studies.

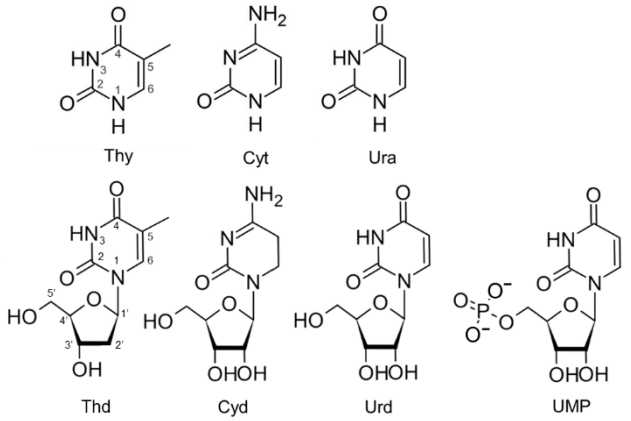

Figure 1. Molecular structures of pyrimidine nucleobases and their derivatives. UMP is doubly charged at the pH value 7.48 employed in the present study.

Experimental

This paper presents the first report of EUV-TRPES of aqueous nucleobases, so that there are a few noteworthy aspects. First of all, EUV pulses generate photoelectrons with high kinetic energies, so that inelastic scattering prior to photoemission can be neglected. This represents a clear difference between EUV-TRPES and UV-TRPES in that the latter requires detailed analysis of scattering effects.[29] In this sense, EUV-TRPES is clearly advantageous. The drawback of EUV-TRPES is that the solvent is ionized by one-photon absorption, so that greater care is needed to avoid space charge effects.[30] This difficulty is mitigated by employing a laser system with a high repetition rate. The driving lasers for generation of UV and EUV pulses in the present study were a 1 kHz Ti:sapphire regenerative amplifier (35 fs, 800 nm, 1 kHz, 6 mJ) for gas-phase experiments and a 10 kHz Ti:sapphire amplifier (35 fs, 800 nm, 10 kHz, 0.7 mJ) for liquid-phase experiments.[31] Some of the liquid-phase experiments were also performed using a Yb:KGW regenerative amplifier (90 fs, 1030 nm, 20 W, variable repetition rate), which was operated at 25-50 kHz. The EUV photon energy was 21.7 eV for gas-phase experiments, and 27.9 or 26.4 eV for solution-phase experiments (only for aqueous Cyd, 21.7 eV was employed). An energy of 21.7 eV was chosen for the gas-phase experiments because it does not ionize the He (ionization energy: 24.59 eV) that was used as a carrier gas for supersonic jets. Further experimental details are described in Supporting Information.

The observed spectra of aqueous solutions exhibit a strong short-lived signal in the electron binding energy (eBE) region above 5 eV; the eBE is the difference between the probe photon energy and the observed electron kinetic energy (eKE). An example for a 0.15 M Cyd aqueous solution is shown

in Figure 2(a). As seen in Figure 2(b), the same feature is found for a 0.05 M NaCl aqueous solution (without any nucleobase). This strong coherent artifact is due to non-resonant (1+1') ionization of solvent water by the UV and EUV pulses, and is observed for all aqueous solutions. Its temporal width depends on the laser system employed in each measurement (Figure S2 in Supporting Information). More specifically, the spectra for Cyd and Urd measured with a cross-correlation time of 60±2 fs (10 kHz Ti:sapphire laser) had a narrower temporal width than that for Ura,UMP, Thy, and Thd measured with a cross-correlation time of 100±3 fs (Yb:KGW laser). This component (Figure 2(b)) can be removed by subtracting the distribution of coherent artifact from pump-probe spectra. Otherwise, the coherent artifact can be easily identified and removed using a Gaussian function in the global fitting analysis, because the artifact always appears as a Gaussian function centered at the time origin.

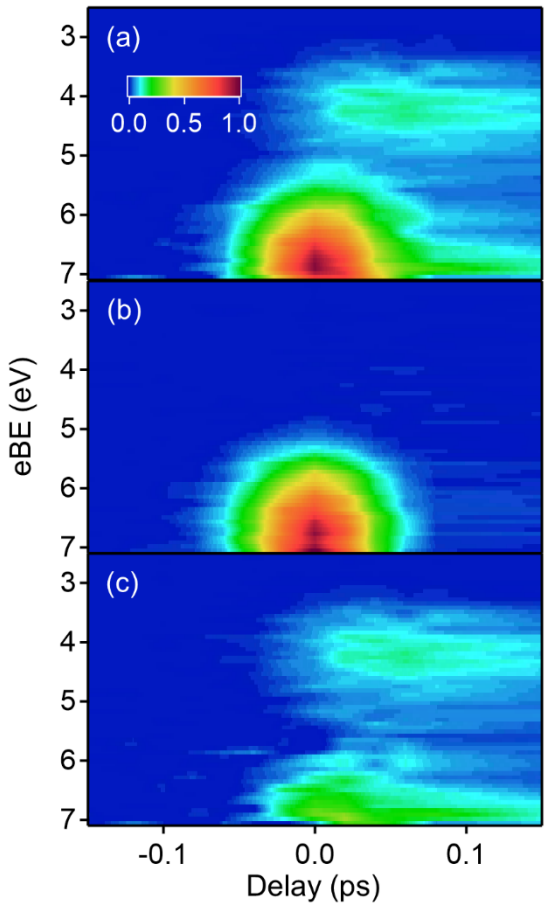

Figure 2. Subtraction of coherent artifact from raw pump-probe photoelectron spectra. (a) Raw data for 0.15 M Cyd aqueous solution, (b) coherent artifact measured for 0.05 M NaCl aqueous solution, (c) spectrum after subtraction of (b) from (a).

The penetration depths of the pump (267 nm) and probe (57 nm) radiation are estimated to be 3 μm and 20 nm for aqueous 0.15 M Urd solution, respectively. However, the probing depth of photoelectron spectroscopy is primarily limited by the escape depth for electrons, which is limited by electron scattering in the liquid. The probing depth is not accurately known but is estimated to be on the

order of 1-2 nm for EUV-TRPES. Thus, the photoelectron signal intensity reflects the local concentration at the gas-liquid interface. Hydrophobic molecules tend to become concentrated on the liquid surface, producing a higher photoelectron signal intensity than that for hydrophilic molecules. Ura is the most hydrophobic among the compounds studied here, and the largest surface enrichment factor is anticipated for it. However, its low bulk solubility provides an extremely low signal intensity. UMP, being the most hydrophilic with the least degree of surface enrichment, produces the lowest signal intensity at any concentration; however, UMP is much more soluble than Ura in water, thus producing a stronger photoelectron signal. To quantitatively discuss these differences, we measured the EUV one-color photoelectron signal intensity as a function of the bulk concentration (Figure 3(a)). In a previous study, Nishitani et al. demonstrated that the EUV photoelectron signal intensity has a strong correlation with the surface concentration estimated from surface tension measurements.[30] Photoelectron spectroscopy measurements allow estimation of the (relative) surface concentration with a higher sensitivity than surface tension measurements, and it can be performed for a non-stationary liquid surface under vacuum. Figure 3(a) shows that the photoelectron signal intensity for UMP is lower than that for Urd at the same concentration. No clear indication of saturation is seen in the concentration dependence for the three compounds. For comparison with our experimental results, we performed molecular dynamics simulations to estimate the depth profiles for Ura, Urd, and UMP in aqueous solutions, as shown in Figure 3(b). The computational conditions are described in Supporting Information (Section II.F). The calculated depth profiles agree with the trend observed experimentally.

The absolute values of eBE were calibrated using the value of 11.3 eV for liquid water as an internal energy standard;[32] therefore, these values are free from the influence of surface dipole moments.[31]

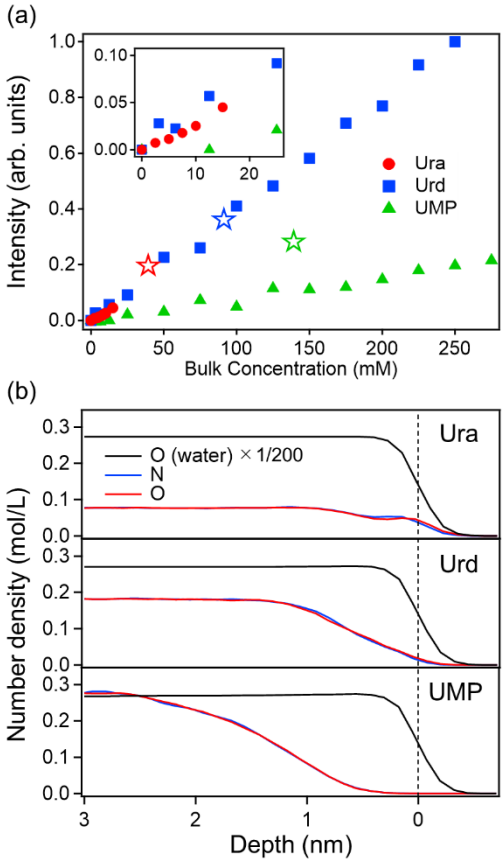

Figure 3. (a) Concentration dependence of photoelectron signal intensity for Ura, Urd, and UMP. The intensity is normalized by the spectral area for H_2O $1b_1$ in the liquid phase and scaled to unity using the intensity for 250 mM Urd. The inset shows an enlarged view of the low-concentration region. (b) Depth profiles at the gas-liquid interfaces computed for aqueous solutions of 39 mM Ura, 91 mM Urd, and 139 mM UMP. The dashed vertical line indicates the Gibbs dividing surface. Ura and Urd are electrically neutral, while UMP is doubly negatively charged and electrically balanced with the counter ions of Na^+. The blue and red lines indicate the number densities of nitrogen and oxygen atoms in pyrimidine rings, respectively, which are greater than the molecular density by a factor of two. Note that the density of solvent water is shown by a factor of 1/200. The stars in (a) indicates the integrated population within 2 nm from the Gibbs dividing surface calculated from the depth profiles computed for Ura, Urd and UMP. The relative intensities are in fair agreement with the experimental results.

Results

(a) Aqueous Cyd

According to quantum chemical calculations, Cyd has two $^1\pi\pi^*$ states in the UV region.[33] The 267 nm pump pulses possibly excite both of these states, but this does not alter the following discussion. Ma et al. performed a fluorescence up-conversion (FU) and TAS study on the excited-state dynamics of Cyd for 267 nm photoexcitation, and estimated the quantum yield for $^1n\pi^*$ to be 0.49±0.05.[14] This was slightly higher than the value of 0.33±0.05 for deoxycytidine (dCyd).[14] IR-TAS of aqueous dCyd

indicated a vibrational transition at 1574 cm^{-1};[34] the lifetime (37±4 ps) estimated for this band agrees with one of the time constants observed for ground-state bleach recovery (35±2 ps).[14]

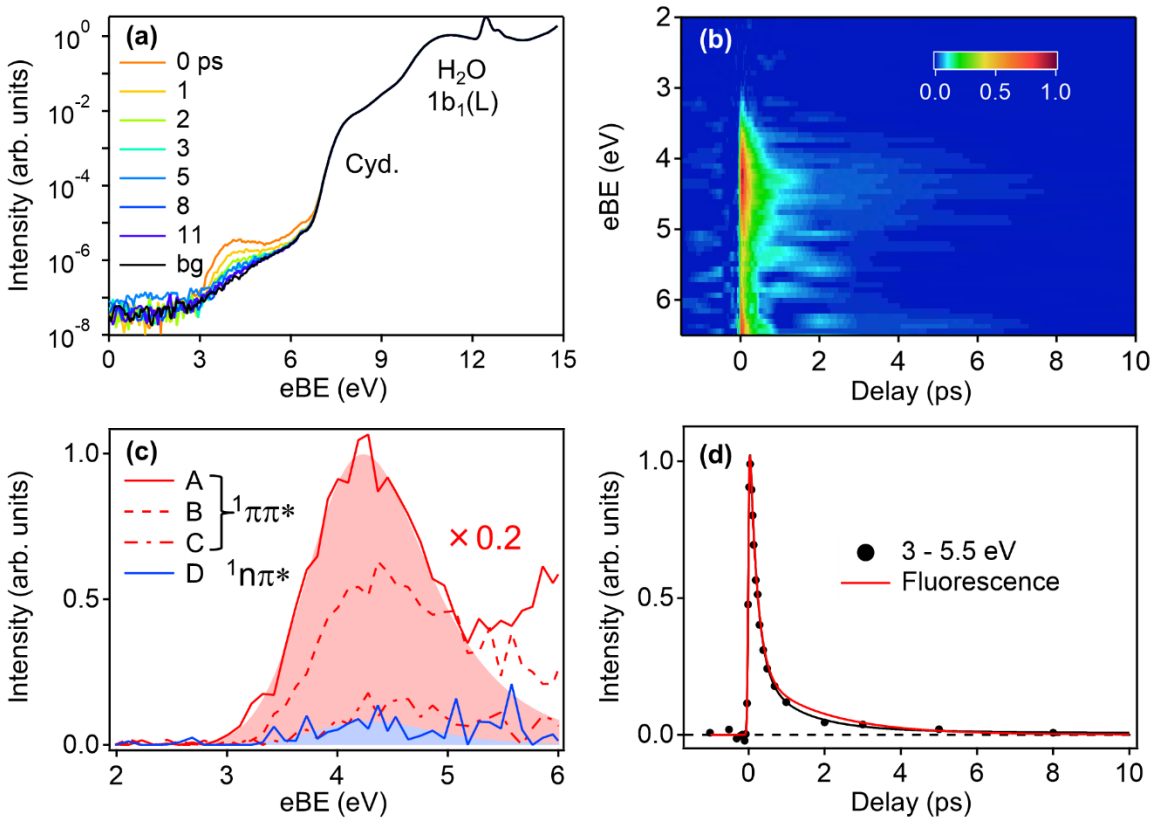

Figure 4. Time-resolved photoelectron spectra of aqueous 0.15 M Cyd solution obtained using 267 nm pump and 21.7 eV probe pulses. (a) Overview of spectra including strong peaks for liquid (11.3 eV) and gaseous water (12.6 eV). (b) Two-dimensional time-energy map of photoelectron spectra below eBE of 6.5 eV. A coherent artifact at the time origin has already been subtracted. The strong short-lived signal is associated with $^1\pi\pi^*$ state. The photoelectron spectrum for each delay time was integrated over 2.04×10^7 shots. The spectra were measured at unevenly spaced 31 delay times between -2 to 29 ps and linearly interpolated with an interval of 11 fs. (c) The results of global fitting analysis. The spectra associated with the $^1\pi\pi^*$ (red solid, dashed, and dash-dotted line) and $^1n\pi^*$ states (blue solid) are shown; the intensity of the $^1\pi\pi^*$ spectrum is shown on a five times smaller scale. (d) Time profiles of photoelectron signal intensity integrated over selected eBE regions of 3-5.5 eV (black dots) and the fluorescence decay profile reconstructed from the time constants and amplitudes previously reported in Ref. [35] with our instrumental resolution of 0.06 ps (red). The black solid curve is the result of the global fitting analysis.

Figure 4(a) shows time-resolved photoelectron spectra measured for an aqueous 0.15 M Cyd solution using 267 nm pump and 21.7 eV probe pulses. The horizontal axis indicates the eBE. The strong signal seen at 12.6 eV is due to one-photon ionization of gaseous water evaporated from the liquid surface. The broad peak at 11.3 eV is due to liquid water, and an EUV-induced one-photon ionization

peak for Cyd appears at around 8 eV. The pump-probe photoelectron signal for aqueous Cyd is seen at 4 eV with an intensity six orders of magnitude smaller than the one-photon ionization signal for solvent water. This large difference in signal intensity reflects the difference in the number density of photoexcited Cyd and (unexcited) solvent water molecules. The number density of water molecules is two orders of magnitude greater than that of Cyd in aqueous solution. Additionally, attenuation of the pump pulses to avoid one-color UV-induced multiphoton ionization reduced the excitation efficiency for Cyd to less than 1%. As seen in the figure, the eBE region above 6.5 eV is dominated by strong EUV-induced photoelectron signals due to unexcited Cyd and solvent water. Thus, we will focus on the eBE region below 6.5 eV.

Figure 4(b) shows a two-dimensional time-energy map of the pump-probe signal. A coherent artifact has already been subtracted. The spectra exhibit a prominent band in the eBE regions of 3.0-5.5 eV, which is assigned to photoionization from optically excited $^1\pi\pi^*$ state to the ground cationic state (D_0: π^{-1}) for the following reasons. The vertical excitation energy from S_0 to $^1\pi\pi^*$ is estimated to be 4.6 eV based on the peak wavelength (269 nm) of the UV absorption spectrum of aqueous Cyd. The vertical ionization energy from S_0 to D_0 of aqueous Cyd is 8.1 eV.[36] Photoionization from $^1\pi\pi^*$ state occurs to D_0. Therefore, the eBE in the Franck-Condon region for $^1\pi\pi^*$ state is estimated to be 3.5 eV, which agrees reasonably well with the observed band position. The entire photoelectron signal at 3-6.5 eV appears at the time origin, and no clear spectral shift is identified; this is consistent with the small dynamic Stokes shift previously observed for $^1\pi\pi^*$ states of aqueous Cyd using TAS.[14]

We performed a global fitting analysis of the photoelectron spectra by assuming a sequential relaxation process of A→B→C→D and the relaxation from all of these states to S_0 (see Supporting Information for more details). The analysis provided the lifetimes for A, B, C, and D to be 0.07±0.01, 0.21±0.02, 1.3±0.3 and 6±1 ps, respectively and the state-associated spectra as shown in Figure 4(c). The spectra determined for A, B and C are essentially the same, suggesting that they are all $^1\pi\pi^*$ state; the smallest time constant is considered to be an effective lifetime in the Franck-Condon region and 0.21 and 1.3 are regarded as the biexponential decay time constants for the $^1\pi\pi^*$ state after vibrational motions. Furthermore, we found that the time profile of the photoelectron signal intensity integrated over 3.0-5.5 eV is very similar to the fluorescence decay profile previously measured using the FU method,[35] as shown in Figure 4(d). Assuming a bi-exponential function of the form

$$f(t) = \alpha\exp(-t/\tau_1) + (1-\alpha)\exp(-t/\tau_2),$$

the FU measurements provided $\alpha = 0.83, \tau_1 = 0.18$ and $\tau_2 = 0.92$ ps with an instrumental resolution of 0.45 ps.[35] A more recent study gave values of $\alpha = 0.79 - 0.86, \tau_1 = 0.24$ and τ_2 =1.79 ps (α varied slightly with probe wavelength).[14] These time constants are in excellent agreement with the aforementioned values determined by global fitting of our spectra. Since fluorescence originates from the optically bright $^1\pi\pi^*$ state, the agreement between the EUV-TRPES and FU results suggests that the photoelectron signal is primarily associated with $^1\pi\pi^*$ state. The appearance of the photoelectron spectra associated with $^1\pi\pi^*$ and $^1n\pi^*$ in Figure 4 (c) are rather broad, indicative of the presence of multiple bands. We performed least-squares fitting of the spectra by assuming two exponentially modified

Gaussian (EMG) functions and estimated the $^1n\pi^*$ quantum yield to be 0.02, which, however, is too small to determine precisely in the present study (Figures S6). Our result is consistent with the computational study on aqueous dCyd, which indicated that $^1n\pi^*$ plays a minor role in the deactivation from $^1\pi\pi^*$.[33] Further investigation with different pump wavelengths is of interest[15] but is beyond the scope of the present study.

(b) Aqueous Urd

Figure 5(a) shows EUV-TRPES results for Urd in a phosphate buffer (PB) using 267 nm pump and 27.9 eV probe pulses. A coherent spike in the original experimental data and a weak background signal due to photoionization of PB have already been subtracted. Similar to the case for Cyd, we focus on the eBE region below 7 eV. A short-lived signal from $^1\pi\pi^*$ state can be clearly identified in the sub-picosecond region. In addition, a long-lived signal is discernible in the eBE region of 5-6 eV, particularly in the enhanced plot in Figure 5(b). This signal is assignable to $^1n\pi^*$ state. Closer examination of this photoelectron signal reveals an energy shift toward higher eBE by about 0.5 eV within 10 ps, which is indicative of either structural relaxation in the $^1n\pi^*$ state or intersystem crossing (ISC) to the triplet manifold. We performed a global fitting analysis by assuming sequential two-step relaxation via $^1n\pi^*$, and determined the decay time constants of $^1\pi\pi^*$ and $^1n\pi^*$ to be 0.12±0.02 and 5±1 ps, respectively. The extracted spectra are shown in Figure 5(c). A computational study by Pepino et al. indicated that hydrated Urd in the $^1n\pi^*$ state undergoes structural deformation between a planar (4.84 eV) and a twisted structure (4.43 eV);[37] however, this deformation would occur in less than 5 ps. On the other hand, the $^1n\pi^*/^3\pi\pi^*$ spin-orbit coupling is reasonably large (42 cm^{-1}),[37] and the computed minimum energy (3.2 eV)[37] for $^3\pi\pi^*$ state provides an eBE of about 5 eV in reasonable agreement with the observed energy. Therefore, the spectral evolution that occurs with the time constant of 5 ps is assigned to $^1n\pi^*\rightarrow{}^3\pi\pi^*$ ISC. This also accords with the fact that gaseous Thy and Ura exhibit efficient ISC from $^1n\pi^*$ to $^3\pi\pi^*$, as discussed later.

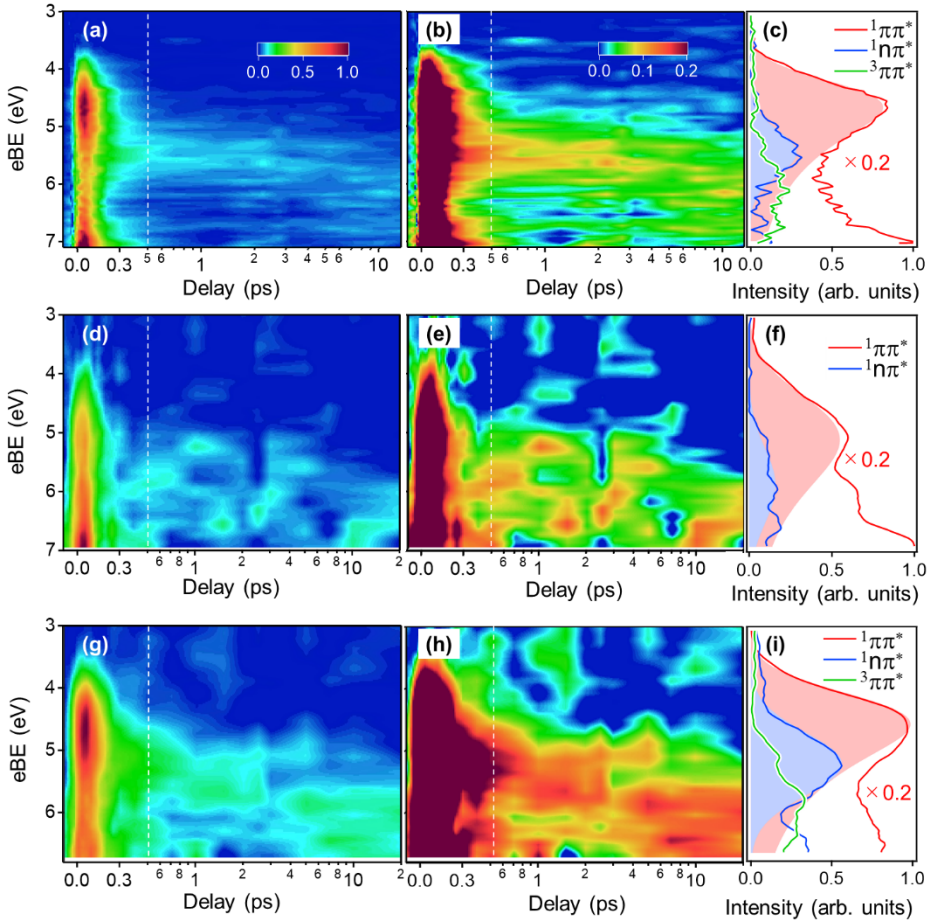

Figure 5. Photoelectron spectra of (a) 0.15 M Urd, (d) 0.01 M Ura, and (g) 0.15 M UMP in PB. The pump and probe pulses are 267 nm and 27.9 eV for Urd, and 257 nm and 26.4 eV for Ura and UMP, respectively. Plots using an enhanced intensity scale are shown in (b), (e), (h). The horizontal axis is linear up to 0.5 ps and logarithmic thereafter. A weak long-lived signal is discernible in all cases. The spectra were measured at 32 unevenly spaced delay times between -2 to 13 ps for Urd and 30 delay times between -2 to 20 ps for Ura and UMP, and linearly interpolated with an interval of 11 fs. The photoelectron spectra for each time delay are integrated over 1.356×10^7, 8.62×10^7, and 8.175×10^7 shots for Urd, Ura, and UMP, respectively. The data for Ura and UMP were subjected to boxcar smoothing with window widths of 0.7 and 0.5 eV, respectively, in order to clarify major features; the original data are shown in Figure S4 in Supporting Information. A global fitting analysis was performed to extract the spectra associated with the $^1\pi\pi^*$ (red solid line), $^1n\pi^*$ (blue solid) and $^3\pi\pi^*$ (green solid) states for Urd, Ura, and UMP, as shown in (c), (f) and (i), respectively; the intensity of the $^1\pi\pi^*$ spectrum is shown on a five times smaller scale. The spectrum associated with the $^1\pi\pi^*$ and $^1n\pi^*$ states involve multiple bands, so that the shaded region was determined as a single photoelectron band in order to evaluate the quantum yield of $^1n\pi^*$ using EMG functions (see section II.C in Supporting Information).

If we assume that the ionization cross-sections for $^1\pi\pi^*$ and $^1n\pi^*$ are equal, the quantum yield for $^1n\pi^*$ can be determined from the integrated spectral intensities of the $^1n\pi^*$ and $^1\pi\pi^*$ bands. It should

be noted that intensity must be evaluated for a single photoelectron band for each ionized state. We performed least-squares fitting of the spectrum by assuming two Gaussian functions or two EMG functions and estimated the $^1n\pi^*$ quantum yield for Urd to be 0.04-0.06 (Figures S7).

A recent TAS and computational study estimated the lifetime of $^1\pi\pi^*$ states in Urd to be 97 fs (our value 120 fs), and the quantum yield for the long-lived component to be < 0.2.[18] The yield (< 0.06) obtained in the present study is significantly lower. Another related process, an intramolecular sugar-to-base charge transfer mechanism, has also been proposed for purine nucleobases; however, it has been theoretically ruled out for pyrimidine nucleobases by Pepino et al. due to unfavorable energetics.[37]

(c) Aqueous Ura

Figure 5(d) shows EUV-TRPES results for Ura in PB measured using 257 nm pump and 26.4 eV probe pulses. A short-lived signal associated with $^1\pi\pi^*$ state can be clearly identified, together with a very weak long-lived component assignable to $^1n\pi^*$ state. In the enhanced plot in Figure 5(e), a long-lived component is visible at around 5-7 eV, which shows little variation with time. Global fitting gives a time constant of 67±3 fs for $^1\pi\pi^*$ state. FU previously estimated the lifetime of $^1\pi\pi^*$ state to be 96 fs with an instrumental temporal resolution of 330 fs.[38] A TAS study using sub-10 fs pulses found that the decay time varies from 54 to 128 fs depending on the probe wavelength in the range of 4.35-4.76 eV;[39] the average value of the decay time is in fair agreement with the FU and EUV-TRPES results. Several TAS studies also reported the presence of a picosecond component, but its origin has not been fully established.[6, 18, 39] We performed the least-squares fitting of the spectra associated with $^1\pi\pi^*$ and $^1n\pi^*$ states shown in Fig. 5(f) with two Gaussian functions or two EMG functions and estimated the $^1n\pi^*$ quantum yield for Ura to be 0.04-0.06. (Figure S8)

(d) Aqueous UMP

Figure 5(g) shows EUV-TRPES results for UMP in PB measured using 257 nm pump and 26.4 eV probe pulses. A short-lived photoelectron signal associated with the $^1\pi\pi^*$ state and a long-lived component can be clearly identified. Although the long-lived component is slightly stronger than that for Urd, as seen in Figure 5(h), the results for UMP are very similar to those for Urd. The signal decays with two time constants of 0.095±0.003 and 1.2±0.2 ps, which are ascribed to $^1\pi\pi^*$ and $^1n\pi^*$, respectively. The yield of $^1n\pi^*$ was estimated to be 0.07 by fitting the spectra shown in Figure 5(i) using two EMG functions; the estimated upper bound is 0.15. (Figure S9)

(e) Aqueous Thd and Thy

The TAS study reported the quantum yield for $^1n\pi^*$ in aqueous Thy and Thd to be 0.11±0.13 and 0.14±0.04, respectively.[6] These molecules call particular attention because formation of Thy dimer is one of major photochemical damages for DNA. Multiple UV-TRPES studies have been previously applied to these systems, but they found no signal for $^1n\pi^*$ and concluded that $^1n\pi^*$ is not involved in the relaxation process.[11, 13] Thus, we applied EUV-TRPES to these systems to examine whether the

actual $^1n\pi^*$ quantum yields are considerably smaller than the estimates by TAS.

Figures 6(a) and 6(c) show EUV-TRPES results for Thd (150 mM) and Thy (10 mM) in PB measured using 257 nm pump and 26.4 eV probe pulses, respectively; a long-lived component is clearly seen in both cases. A short-lived signal associated with the $^1\pi\pi^*$ state exhibits a rapid spectral shift, indicating that complex structural dynamics are operative. We performed a global fitting analysis of the spectra by assuming four components to express the energy shift; the extracted time constants for Thd are 0.087±0.003 and 0.25±0.01 ps for the $^1\pi\pi^*$ state and 3.1±0.2 ps for the $^1n\pi^*$ state. The $^1n\pi^*$ quantum yield is estimated to be 0.22 from the red-shaded area associated with $^1\pi\pi^*$ and blue-shaded area associated with $^1n\pi^*$ in Fig. 6(b). Surprisingly, the quantum yield was found to be even higher than the value previously estimated using TAS. To investigate the possible formation of molecular aggregates at a high concentration of 150 mM employed for the aforementioned measurements, we also performed experiments using 15 mM Thd in PB, and obtained time constants of 0.13±0.08 and 0.15±0.09 ps for $^1\pi\pi^*$, and 3.4±0.8 ps for $^1n\pi^*$. The estimated $^1n\pi^*$ yield was 0.23. These results suggest that the lifetimes and quantum yield are not strongly influenced by aggregation of nucleobases.[40]

A global fitting analysis for Thy gives time constants of 0.15±0.09 and 0.16±0.09 ps for the $^1\pi\pi^*$ state, and 2.5±0.8 ps for the $^1n\pi^*$ state. The $^1n\pi^*$ quantum yield is estimated to be 0.16 from the global fitting analysis; the estimated upper bound is 0.19. Figure 6(d) compares the time profile of the photoelectron signal intensity integrated over 2.5-6.0 eV and the fluorescence decay profile previously measured using the FU method.[38] The fluorescence decay profile has been characterized with a biexponential decay with the time constants of 0.195 and 0.633 ps, while EUV-TRPES clearly exhibits the presence of a long-lived component.

The photoelectron bands associated with the $^1\pi\pi^*$ states of Urd, Ura and UMP (Figure 5 and S7-S9) are broader than those of Thd and Thy (Figures 6, S10 and S11). It is possible that Urd, Ura and UMP have ultrafast structural deformations that are unresolved with our temporal resolution. As described in the next section, the photoelectron spectra of gaseous Thy and Ura exhibit an ultrafast spectral shift due to structural deformation within 30 fs.

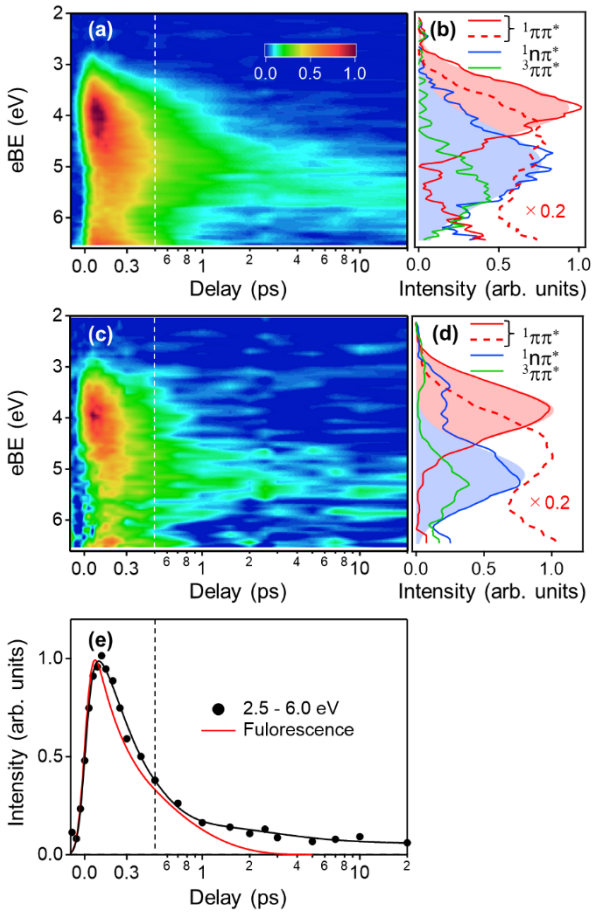

Figure 6. Photoelectron spectra of (a) 0.15 M Thd and (c) 0.01 M Thy in PB. The pump and probe pulses are 257 nm and 26.4 eV, respectively. The horizontal axis is linear up to 0.5 ps and logarithmic thereafter. A weak long-lived signal is discernible in all cases. A global fitting analysis was performed to extract the spectra associated with the $^1\pi\pi^*$ (red solid and dashed lines), $^1n\pi^*$ (blue solid line) and $^3\pi\pi^*$ (green solid line) states for Thd and Thy shown in (b) and (d), respectively; the intensity of the $^1\pi\pi^*$ spectrum is shown on a five times smaller scale. The spectral shift for the $^1\pi\pi^*$ state is expressed by two components. The spectra associated with $^1\pi\pi^*$ and $^1n\pi^*$ states involve multiple bands, so that the shaded region was determined as a single photoelectron band in order to evaluate the quantum yield for $^1n\pi^*$ (see the text). The state-associated spectra in (d) were subjected to boxcar smoothing with the window widths of 0.55 eV in order to clarify major features. The spectra were measured at 30 unevenly spaced delay times between -2 to 20 ps, and linearly interpolated with an interval of 11 fs. The photoelectron spectra for each time delay are integrated over 4.4×10^7 and 5.465×10^7 shots for Thd and Thy, respectively. (e) Time profiles of photoelectron signal intensity of aqueous Thy integrated over selected eBE regions of 2.5-6.0 eV (black dots) and the fluorescence decay profile reconstructed from the time constants and amplitudes previously reported in Ref. [38] with our instrumental resolution of 0.1 ps (red). The black solid curve is the result of the global fitting analysis.

(f) Gaseous Thy

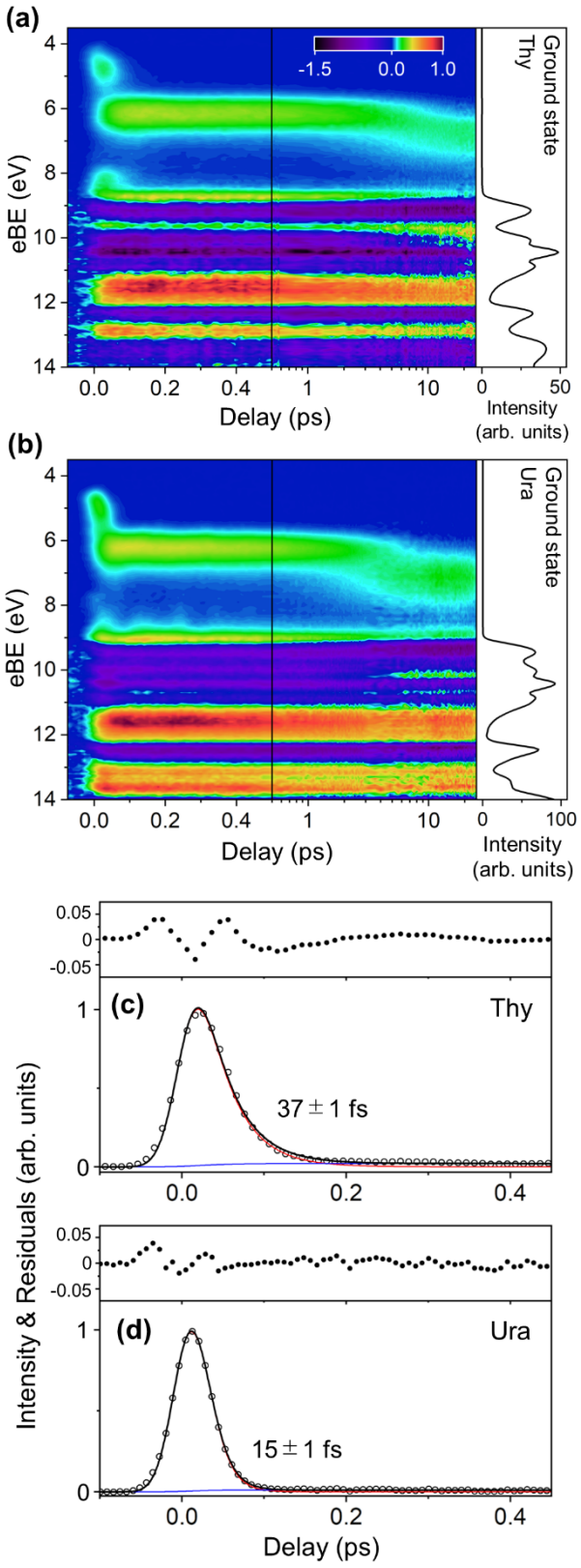

Figure 7. Two-dimensional map of photoelectron spectra measured for gaseous (a) Thy and (b) Ura using 267 nm pump and 21.7 eV probe pulses. The horizontal axis is linear up to 0.5 ps and logarithmic thereafter. Shown on the right are photoelectron spectra at thermal equilibrium. It can be seen that the

bleached regions in the two-dimensional map coincide with peaks in the thermal-equilibrium spectrum. The signal from photoexcited $^1\pi\pi^*$ state rapidly decays to create a $^1n\pi^*$ signal, which changes to a $^3\pi\pi^*$ signal on a picosecond timescale. Intensity of signal integrated over eBE region of 3.6-5.2 eV for gaseous Thy and 4.0-5.4 eV for gaseous Ura are shown in (c) and (d), respectively. Measured data points are shown as open circles, and short-lived and long-lived components are shown as red and blue lines, respectively. The sum of these components is shown as a black line. The upper panel shows residuals.

Figure 7(a) shows time-resolved photoelectron spectra of gaseous Thy measured using 267 nm pump and 21.7 eV probe pulses. The positive bands in green and red colors are due to photoexcited states, and the negative bands in black and purple colors are for the ground-state bleach. The adiabatic ionization energy of Thy from S_0 to D_0 is 8.92 eV,[41-43] and the vertical excitation energy for $^1\pi\pi^*$ is estimated to be 4.9 eV; thus, the band in the 4-5 eV region is assigned to ionization from $^1\pi\pi^*$ to D_0. Ultrafast decay of this band is followed by the appearance of a band at around 6 eV, which gradually shifts to higher eBE after several picoseconds. The short delay-time region of this band is ascribed to photoionization from $^1n\pi^*$, while the long delay time region is to $^3\pi\pi^*$. The $^1n\pi^*$ of gaseous Thy is energetically lower than $^1\pi\pi^*$; computational estimates of the $^1\pi\pi^*$-$^1n\pi^*$ energy gap reported so far are scattered from nearly zero to 1 eV, depending on the level of theory. Ionization from $^1n\pi^*$ occurs to the n^{-1} cationic state that is expected at 9.84 eV,[44] which makes the vertical eBE value for $^1n\pi^*$ higher than that for $^1\pi\pi^*$ by approximately 1.5 eV. The adiabatic excitation energy for $^3\pi\pi^*$ was estimated to be 2.9 eV in a previous study,[26] from which eBE is crudely estimated to be 6-7 eV, in reasonable agreement with our observation.

The $^1\pi\pi^*$ signal appears weaker than the $^1n\pi^*$ signal, even though the initial optical transition occurs entirely to the former. This is primarily due to the short lifetime of the $^1\pi\pi^*$ state. We estimated the Dyson norms for photoionization from the $^1\pi\pi^*$ to π^{-1} state and the $^1n\pi^*$ to n^{-1} state using the EOM-CCSD aug-cc-pVDZ level of theory and found them to be equal;[45] the photoionization cross-sections from $^1\pi\pi^*$ and $^1n\pi^*$ are considered to be the same. The $^1\pi\pi^*$ signal in the 3.5-5.4 eV region exhibits a rapid energy shift, which is attributed to nuclear wave-packet motion on the $^1\pi\pi^*$ surface toward the conical intersection with $^1n\pi^*$. As seen in Fig. 7(c), the integrated photoelectron intensity for the $^1\pi\pi^*$ state decays with a time constant of 37±1 fs (Section III.A in Supporting Information).

A number of UV-TRPES studies have been reported for gaseous Thy, as summarized in Supporting Information. Earlier UV-TRPES results hinted at the presence of an ultrashort-lived component within the cross-correlation time of the pump and probe laser pulses; however, a low temporal resolution and the presence of the probe-pump signal hindered unambiguous observation of this component. Recently, Wolf et al. performed TAS in the soft X-ray region[27] and estimated the $^1\pi\pi^*$ lifetime to be 60±30 fs. They also performed TRPES with 14 eV probe pulses, and determined the lifetime to be 80±30 fs.[26] Our estimate of 37 fs is the shortest among all these studies. Early computational simulations at the CASSCF (complete active space self-consistent field) level of theory predicted a picosecond lifetime for $^1\pi\pi^*$, while a recent MRSF-TDDFT (multi-reference spin-flip time-

dependent density functional theory) study that considered dynamic electron correlation predicted the lifetime to be 30 fs, in good agreement with our result.[46] As has already been pointed out by many studies, consideration of dynamic electron correlation is important for accurate estimation of the potential energy barriers for nuclear wave-packet motion in the excited states.[13, 25, 37, 46-47]

The photoelectron band appearing in the eBE region of 8-8.5 eV is also ascribed to photoionization from $^1\pi\pi^*$. This band corresponds to ejection of π electrons from $^1\pi\pi^*$, creating an electronically excited cationic final state. A rapid eBE shift is not seen for the 8-eV band for the $^1\pi\pi^*$ state, presumably because the topographies of the potential energy surfaces are similar for the initial and final states of this particular ionization transition. The signal seen in the region from 8.5 to 9.5 eV is largely due to ionization from the $^1n\pi^*$ and $^3\pi\pi^*$ states.

To investigate the time evolution of the $^1n\pi^*$ and $^3\pi\pi*$ state, we performed global fitting to extract the decay time constants and the spectra shown in Figure S18 in Supporting Information. Although the global fitting cannot express an energy shift for $^1\pi\pi^*$ around 4.0-5.5 eV, they provide a time constant for $^1\pi\pi^*$ (39 fs) that is consistent with the least-squares fit shown in Fig. 7(c). The $^1n\pi^*$ signal intensity exhibited dual components: a rapid initial decay (τ_b: 0.28±0.01 ps) and a more gradual decay (τ_c: 5.79±0.04 ps). The integrated signal intensity for $^3\pi\pi^*$ is slightly smaller (86%) than that for $^1n\pi^*$, indicating that the quantum yield for ISC is 0.86. The lifetime for $^3\pi\pi^*$ is longer than 30 ps and is undetermined in the present study. The presence of two time constants for $^1n\pi^*$ means either that there are two dynamical processes, or the photoionization cross-section is affected by electronic or structural variations. We evaluated the quantum yield for $^1n\pi^*$ from the initial photoelectron signal intensity prior to the slow decay; this yielded a quantum yield of approximately unity. The ground-state bleach signal seen above 9 eV is discussed later.

(g) Gaseous Ura

Figure 7(b) shows time-resolved photoelectron spectra of gaseous Ura measured using 267 nm pump and 21.7 eV probe pulses. Ura and Thy have almost identical structures, being different only in the presence of a methyl group in the latter. As summarized in Supporting Information, a previous UV-TRPES study of Ura using 267 nm pump and 295 nm probe pulses observed a tri-exponential decay profile with time constants of 170 fs, 2.35 ps, and >1 ns.[9] Computational simulations of Ura based on the second-order algebraic-diagrammatic-construction (ADC(2)) method predicted the $^1\pi\pi^*$ lifetime to be 161±40 fs.[16] More recent calculations and TRPES results reported by Chakraborty et al. indicated a substantially shorter $^1\pi\pi^*$ lifetime of 30 fs.[25] The calculations (XMS-CASPT2) considering dynamical electron correlation predict a lower potential hump separating the Franck-Condon region and the conical intersection region, predicting a shorter relaxation time. A similar lifetime has also been obtained using MRSF-TDDFT.[48] Although it is not readily discernible in Fig. 7(b), the $^1\pi\pi^*$ lifetime for Ura is even shorter than that for Thy. The signal intensity integrated over 4-5.4 eV decays in 15±1 fs (Figure 7(d)), and the global fitting analysis provides time constants of 17±1 fs, 0.44±0.01 ps, 3.48±0.03 ps and >30 ps (Figure S19).

Another interesting difference between Ura and Thy is that EUV-TRPES reveals an oscillatory signal in the region of 8-8.5 eV. This signal is assigned to photoionization from $^1n\pi^*$ to an excited cationic state, similar to the case for Thy discussed earlier. We extracted this oscillatory feature and performed a Fourier analysis, as shown in Fig. 8. The results indicated vibrational frequencies of 135 and 315 cm^{-1}. These vibrational modes have not been assigned yet; however, the latter frequency is similar to the one observed by sub-10 fs TAS.[39]

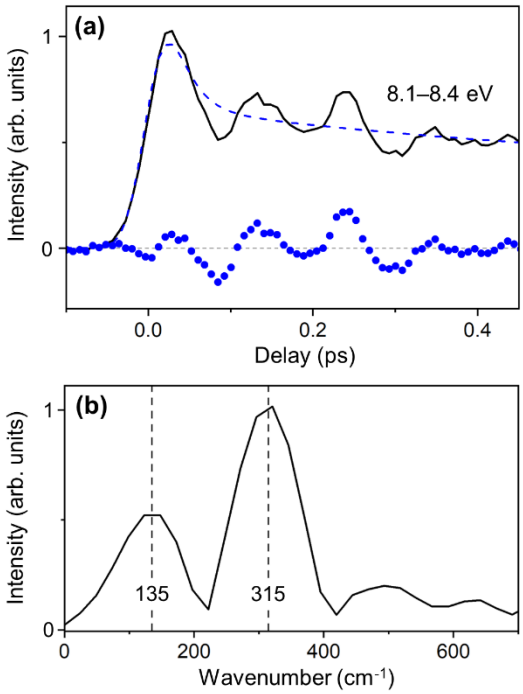

Figure 8. (a) Photoelectron signal intensity for Ura integrated over eBE region of 8.1-8.4 eV. Experimental data and least-squares fits assuming four exponential decay components are indicated by the black solid line and blue dashed line, respectively. The residuals are shown as blue dots. (b) Fourier transform of oscillatory components shown as residuals in (a).

The most direct proof of the ultrafast internal conversion in Ura is observation of ground-state bleach recovery. The recovery signal should appear as a rapid reduction of the bleach depth. Figure 9 shows the photoelectron signal intensity at multiple eBE values where recovery is anticipated. It can be seen that bleach recovery seems to occur for Ura but not for Thy. As mentioned earlier the excitation efficiency with the pump pulses is less than 1%, so that the ground-state bleach depth is very small and influenced by fluctuation of the background signal from unpumped ground-state molecules. Thus, our experimental spectra in high eBE region appear rather noisy; however, Fig. 9 seems to support our claim of the presence of ultrafast internal conversion to S_0 in gaseous Ura.

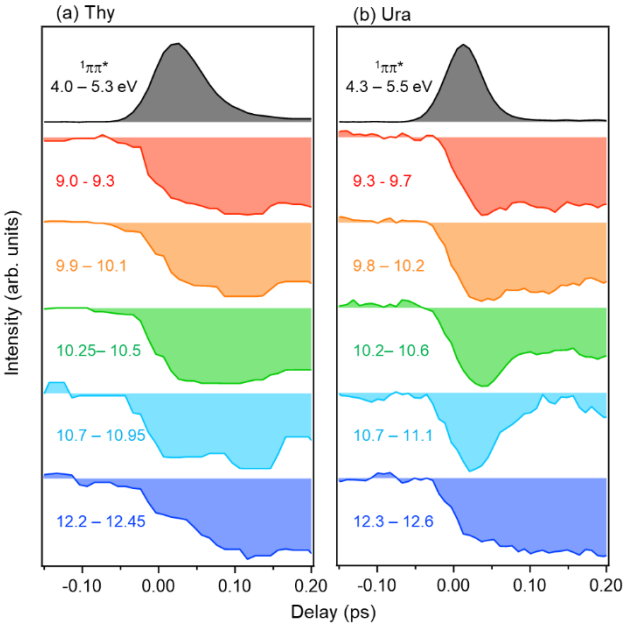

Figure 9. Photoelectron signal intensity integrated over eBE regions where bleach recovery is anticipated as function of delay time. The intensities for (a) Thy and (b) Ura were calculated from the data shown in Fig. 7(a) and (b), respectively.

Discussion

(a) Is the $^1n\pi^*$ quantum yield as high as that estimated using TAS?

The lifetimes and quantum yields estimated in the present study are summarized in Table 1 along with the results of some previous experimental and theoretical studies. Our EUV-TRPES results indicate that the quantum yields for $^1n\pi^*$ in deactivation processes for aqueous Cyd and Ura derivatives are less than 0.1, suggesting that previous estimates based on TAS involve large errors.

Previous TAS studies have identified the presence of a slow relaxation channel via $^1n\pi^*$ or $^3\pi\pi^*$ in aqueous nucleobases; however, a limited temporal resolution hampered accurate estimates of the quantum yields for these dark states. Our EUV-TRPES results clearly indicate that internal conversion from $^1\pi\pi^*$ to S_0 in aqueous Cyd and Ura derivatives occurs within 60–260 fs, which are shorter than the typical temporal resolution of TAS (150–350 fs). Furthermore, the TAS signal around the time origin is obscured by a coherent artifact, limiting the shortest delay time for observation. It is also noted that there is an inherent difficulty in estimating the quantum yield for ultrafast internal conversion by the bleach-recovery measurements. A photoabsorption spectrum of highly vibrationally excited (hot) molecules produced by internal conversion exhibits an enhanced and diminished intensity in the red and blue regions with respect to the absorption maximum, respectively. However, the entire spectrum is not largely changed from that of molecules at the thermal equilibrium, because the vibrational potentials of the upper and lower electronic states are similar for many normal modes, inducing vibronic transitions between the levels with similar vibrational quantum numbers (vibrationally

diagonal transitions). Examples of the absorption spectra of hot molecules can be found in Ref. [49]. Moreover, as shown in Figure 10, the UV photoabsorption spectra of aqueous nucleobases are continuous, so that spectra of hot molecules inevitably overlap with those of thermal molecules; there is no probe wavelength at which photoabsorption by hot molecules can be neglected. Therefore, a part of the bleach recovery occurs immediately at any probe wavelength when internal conversion occurs from the $^1\pi\pi^*$ state; the larger the spectral overlap between the hot and thermal molecules, the larger becomes the ultrafast bleach recovery that occurs in the excited state lifetime (Section II.D in Supporting Information). If TAS fails to monitor this ultrafast bleach recovery that occurs in the lifetime of the $^1\pi\pi^*$ state, it would underestimate the yield for direct relaxation to S_0 and overestimate that for slow process via $^1n\pi^*$.

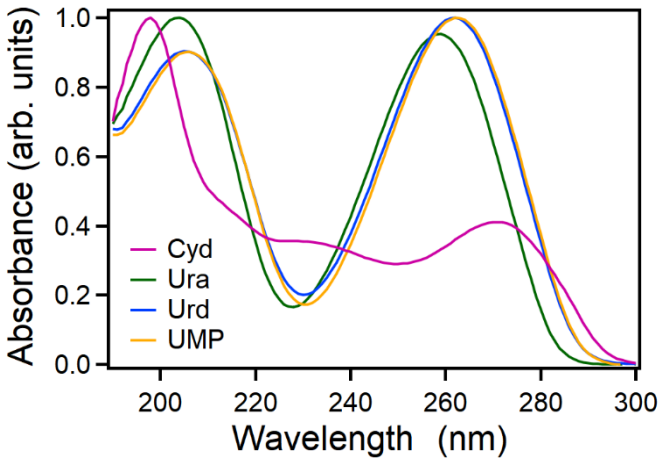

Figure 10. UV photoabsorption spectra of Cyd, Ura, Urd and UMP.

(b) Why was the $^1n\pi^*$ state previously undetected using UV-TRPES?

Previously, aqueous Thy and Thd have been studied using UV-TRPES by Buchner et al.[11] and Erickson et al.[13] with probe photon energies of 5.2 and 6.2 eV, respectively. However, neither of these studies identified a signature of $^1n\pi^*$, as was found using TAS. Our EUV-TRPES measurements identified $^1n\pi^*$ and resolved this apparent contradiction. In fact, we found that the $^1n\pi^*$ quantum yields in aqueous Thy and Thd are the largest among all pyrimidine nucleobases and derivatives studied here.

From the measured eBE distributions, the vertical electron binding energy for the $^1n\pi^*$ states of aqueous Thy and Thd are estimated to be 5.1 and 5.0 eV, respectively. A close comparison of the UV-TRPES results obtained by Buchner et al.[11] and the EUV-TRPES results obtained in the present study reveals generally good agreement, except that the photoelectron spectra measured by Buchner et al. suffer from a significant intensity reduction for eKE of less than 1.0 eV due to reduced electron transmission efficiency for time-of-flight electron energy analyzers in this energy range. Since under the experimental conditions used by Buchner et al.,[11] the $^1n\pi^*$ signal is expected to appear at eKE < 0.7 eV, its detection would be extremely difficult. A similar comparison between the UV-TRPES results of

Erickson et al.[13] and the EUV-TRPES results obtained in the present study indicates that their spectra are energy-shifted towards lower eKE by about 0.5-0.7 eV due to inelastic scattering and/or energy calibration errors. However, the overall spectral profiles measured at delay times of 0.4 and 1.0 ps are in reasonable agreement with our results. The reason why Erickson et al. did not identify a $^1n\pi^*$ signal is most likely due to an insufficient S/N ratio in their measurements. However, even if the $^1n\pi^*$ signal can be identified, accurate estimate of the $^1n\pi^*$ quantum yield is challenging with a probe photon energy of 6.2 eV because it is resonant with electronic transitions of nucleobases, and the signal near the time origin is obscured by overlap of the pump-probe and probe-pump signals.

(c) Does single methylation influence the dynamics?

In the present study, the lifetimes of the $^1\pi\pi^*$ states of Thy and Ura in the gas phase were precisely determined to be 39 and 17 fs, respectively. The former value is in good agreement with the latest computational result (30±1 fs) for Thy considering dynamic electron correlation,[46] while the latter is even shorter than the shortest time constant (30–37 fs) recently computed.[25, 48] The quantum yield for internal conversion to $^1n\pi^*$ was estimated to be about 1.0 (Thy) and 0.45 (Ura) from the photoelectron signal intensities for the $^1\pi\pi^*$ and $^1n\pi^*$ states. Assuming that there are only two deactivation channels for the $^1\pi\pi^*$ state of Ura to $^1n\pi^*$ and S_0, the time constants for the former and latter are calculated to be 31 and 38 fs from the $^1n\pi^*$ quantum yield and $^1\pi\pi^*$ lifetime, respectively. The latter value is in good agreement with the measured value of 39 fs for the formation of $n\pi^*$ in Thy. Thus, the difference between the photophysics of Thy and Ura in the gas phase lies in the latter's extremely fast internal conversion to S_0. Internal conversion from $^1\pi\pi^*$ to $^1n\pi^*$ is through the conical intersection induced by bond-length alternation in a planar geometry,[3, 46] so that methyl substitution will not significantly influence this channel. On the other hand, internal conversion to S_0 occurs via conical intersection induced by out-of-plane deformation caused by the C=C twisting and pyramidalization at C5 carbon atom,[1, 3, 38, 50] similarly with internal conversion from $^1\pi\pi^*$ in ethylene.[51] Methylation increases the moment of inertia for the C=C twist and hinders the internal conversion to S_0; electronic structure calculations at the MS-CASPT2 level of theory predicted that the methyl group at C5 provides a rather small influence on the excited-state potential energy barrier, suggesting the inertia effect.[52]

On the other hand, as for the internal conversion from $^1\pi\pi^*$ to S_0 in an aqueous solution, the difference between Urd and Thd cannot be attributed solely to the inertia effect of the methyl group; solvation dynamics are expected to play a role. According to computational dynamical simulations reported by Borrego-Varillas et al., aqueous Urd has only a negligible potential energy barrier between the $^1\pi\pi^*$ minimum and the $^1\pi\pi^*/S_0$ conical intersection while aqueous 5-methyluridine (5mUrd) has a higher barrier.[18] This barrier height for aqueous 5mUrd is reduced by the structural relaxation of a hydration shell; however, it requires a certain time for the solvent response. We anticipate that aqueous Thd experiences a high potential barrier to reach the conical intersection when the favorable dynamic solvent response has not occurred for the movement of a bulky methyl group. The minimum energy reaction path for internal conversion in Thd in solution likely involves displacement along the

intermolecular coordinates. Thus, a single methylation effect in aqueous solution likely has multiple dynamical origins. Regarding the methylation effect, Gustavsson et al. have previously reported interesting experimental results.[38] They investigated 11 Ura derivatives using FU and found that the fluorescence lifetime (97±3 fs) of aqueous 6-methyluracil is similar to 96±3 fs of Ura, while 5-fluorouracil (694±56 fs) , 5-chlorouracil (155±10 fs) and Thy (195±17 fs) exhibit considerably longer lifetimes. The observed difference between 6-methyluracil and Thy is noteworthy; it proves an important role of the motion of the methyl substituent at C5. The quantum yield for $^1n\pi^*$ in aqueous solution is considerably smaller than those in the isolated molecular condition. This is attributed to destabilization of $^1n\pi^*$ by hydrogen bonding (Table 4 in Ref. 1), which makes $^1n\pi^*$ much less important for deactivation of aqueous nucleobases from $^1\pi\pi^*$. However, the upper bound for the quantum yield of $^1n\pi^*$ reaches as high as 0.22 for aqueous Thd, which is attributed to the aforementioned hindrance of the internal conversion to S_0.

It is interesting to perform EUV-TRPES with a high temporal resolution on various nucleobase derivatives in aqueous and isolated molecular conditions to gain further mechanistic insights into the non-adiabatic dynamics and solvent effects on the photophysics/photochemistry of these building blocks for life. These measurements are in progress in our laboratory.

Conclusion

In the present study, we investigated the pathways and branching ratios for ultrafast electronic relaxation from the $^1\pi\pi^*$ state of aqueous pyrimidine nucleobases using EUV-TRPES. We found that the quantum yields for $^1n\pi^*$ previously estimated for aqueous Cyd (0.49), Ura (0.28) and UMP (0.42) by TAS are incorrect; they are below 0.1. The discrepancies between the results obtained by TAS and EUV-TRPES likely stem from the difficulty of precise measurement of ground-state bleach recovery with a limited temporal resolution, and non-negligible overlap of the photoabsorption spectra of vibrationally excited and thermally equilibrated ground-state molecules. To further investigate this problem, we are planning to revisit UV and IR TAS of these molecules in aqueous solutions. A previous discrepancy in that observation of a long-lived $^1n\pi^*$ state by TAS was not corroborated using UV-TRPES is attributed primarily to specific experimental problems in these UV-TRPES studies. The present study confirmed that the $^1\pi\pi^*$ state of aqueous pyrimidine nucleobases has two relaxation paths, a direct one to S_0 and an indirect one via $^1n\pi^*$ and $^3\pi\pi^*$ states.

Our study uncovered that the most important difference between the dynamics of gaseous Ura and Thy lies in the ultra-short timescale of less than 30 fs that was previously experimentally inaccessible. The difference arises from hindrance of internal conversion to S_0 by a single methylation at the C5 position. The same single methylation effect is seen for aqueous Thy/Thd and Ura/Urd. The former has a longer $^1\pi\pi^*$ lifetime and a higher $^1n\pi^*$ yield than the latter; the yield in Thd is about three times greater than in Urd. In terms of photostability, Thy is considered to be more vulnerable to UV radiation than others. It is interesting to elucidate how this property is related to the thymine dimer formation. Our experimental results clearly indicate the necessity of further accurate and extensive

computational simulations of isolated/aqueous nucleobases on an ultrashort timescale in order to understand their photophysics.

ASSOCIATED CONTENT

Supporting Information.

The Supporting Information is available free of charge on the ACS Publications website at DOI: .
Further information on experimental methods; analysis of the TRPES data; and molecular dynamics simulations (PDF).

AUTHOR INFORMATION

Corresponding Author

***Toshinori Suzuki** − *Department of Chemistry, Graduate School of Science, Kyoto University, Kyoto 606-8502, Japan; Email: suzuki@kuchem.kyoto-u.ac.jp*

Present Addresses

⊥Nippon Steel Corporation, Nagoya Works, 5-3 Tokaimachi, Tokai City, Aichi 476-8686, Japan
†SŪKEN Publishing Co. Ltd., 2-3-3, Tokyo Head Office, Kanda-Ogawamachi, Chiyoda-ku,Tokyo,101-0052
‡KIOXIA Corporation, Yokkaichi Plant, 800 Yamanoisshiki-cho, Yokkaichi-shi, Mie 512-8550, Japan

Funding Sources

This research was supported by JSPS KAKENHI Grant Number 21H04970.

Notes

The authors declare no competing financial interests.

Acknowledgments

This study was supported by JSPS KAKENHI Grant No. 21H04970. We thank Ryuta Uenishi for quantum chemical calculations.

Table 1 Lifetimes (ps) and quantum yields for excited states of aqueous and gaseous nucleobases

Molecule	Method, Ref	lifetime				IC Yield	
		$^1\pi\pi^*$		$^1n\pi^*$	$^3\pi\pi^*$	$^1n\pi^*$	S_0
Cyd (aqua)	EUV-TRPES (This work)	0.07(1), 0.21(2)	1.3(3)	6(1)		0.02	0.98
	FU[a], 33	0.22(1)	0.96(7)				
	FU, TAS, 14	0.24(3)	1.8(1)	35(2)		0.49(4)	0.50(4)
	UV-TRPES, 12	0.35					
Ura (aqua)	EUV-TRPES (This work)	0.067(3)			>20	0.04-0.06	0.94-0.96
	FU, 38	0.096(3)					
	TAS, 39	0.054-0.128	0.11-1.64				
	TAS, 6		(1.9(1))	(24(2))		0.28(5)	0.68(5)
Urd (aqua)	EUV-TRPES (This work)	0.12(2)		5(1)	>20	0.04 (< 0.06) [b]	0.96 (> 0.94)[c]
	TAS, 53	0.21					
	TAS, 18	0.097				< 0.2	
UMP (aqua)	EUV-TRPES (This work)	0.095(3)		1.2(2)	>20	0.07 (< 0.15) [b]	0.93 (>0.85) [c]
	TAS, 54	0.20(5)		365(20)			
	TAS, 6		(2.3(2))	(147(7))		0.42(6)	0.51(6)
Thy (aqua)	EUV-TRPES (This work)	0.15(9)	0.16(9)	2.5(8)	>20	0.12-0.19	0.81-0.88
	UV-TRPES, 11	0.07(1)	0.41(4)				
	UV-TRPES, 13	0.36(6)					
	TAS, 39	0.068-0.151	0.13-2.21				
	TAS, 6		(2.8(4))	(30(13))		0.11(13)	0.87(13)
	FU, 38	0.20 (2)	0.63(2)				
Thd (aqua)	EUV-TRPES (This work)	0.087(3)	0.25(1)	3.1(2)	>20	0.15-0.22	0.78-0.85
	UV-TRPES, 11	0.12(1)	0.39(1)				
	UV-TRPES, 13	0.39(7)					
	TAS[d], 18	0.10				0.05	
Thy (gas)	EUV-TRPES (This work)	0.039(1)		0.28(1)[e] 5.79(4)	>30	~1.0	~0
	VUV-TRPES, 26	0.08(3)		3.5(3)			
	X-ray TAS, 27	0.06(3)					
	MRSF-TDDFT, 46	0.03(1)		6.10(4)			
Ura (gas)	EUV-TRPES (This work)	0.017(1)		0.44(1)[e] 3.48(3)	>30	0.45	0.55
	XMS-CASPT2, 25	0.03					

[a]dCyd

[b]Upper limit

[c]Lower limit

[d]5-methyluridine

[e]The presence of two time constants for $^{1}n\pi^{*}$ means either that there are two dynamical processes, or the photoionization cross-section is affected by electronic or structural variations.

References

1. Improta, R.; Santoro, F.; Blancafort, L., Quantum Mechanical Studies on the Photophysics and the Photochemistry of Nucleic Acids and Nucleobases. *Chem. Rev.* **2016,** *116* (6), 3540-3593, DOI: 10.1021/acs.chemrev.5b00444.

2. Merchan, M.; Serrano-Andres, L., Ultrafast Internal Conversion of Excited Cytosine via the Lowest ππ* Electronic Singlet State. *J. Am. Chem. Soc.* **2003,** *125* (27), 8108-8109, DOI: 10.1021/ja0351600.

3. Matsika, S., Radiationless Decay of Excited States of Uracil through Conical Intersections. *J. Phys. Chem. A* **2004,** *108* (37), 7584-7590, DOI: 10.1021/jp048284n.

4. Perun, S.; Sobolewski, A. L.; Domcke, W., Conical Intersections in Thymine. *J. Phys. Chem. A* **2006,** *110* (49), 13238-13244, DOI: 10.1021/jp0633897.

5. Crespo-Hernandez, C. E.; Cohen, B.; Hare, P. M.; Kohler, B., Ultrafast Excited-State Dynamics in Nucleic Acids. *Chem. Rev.* **2004,** *104* (4), 1977-2019, DOI: 10.1021/cr0206770.

6. Hare, P. M.; Crespo-Hernandez, C. E.; Kohler, B., Internal Conversion to the Electronic Ground State Occurs via Two Distinct Pathways for Pyrimidine Bases in Aqueous Solution. *P. Natl. Acad. Sci. U. S. A.* **2007,** *104* (2), 435-440, DOI: 10.1073/pnas.0608055104.

7. Barbatti, M.; Aquino, A. J. A.; Szymczak, J. J.; Nachtigallova, D.; Hobza, P.; Lischka, H., Relaxation Mechanisms of UV-Photoexcited DNA and RNA Nucleobases. *P. Natl. Acad. Sci. U. S. A.* **2010,** *107* (50), 21453-21458, DOI: 10.1073/pnas.1014982107.

8. Stange, U. C.; Temps, F., Ultrafast Electronic Deactivation of UV-Excited Adenine and Its Ribo- and Deoxyribonucleosides and -Nucleotides: A Comparative Study. *Chem. Phys.* **2018,** *515*, 441-451, DOI: 10.1016/j.chemphys.2018.08.031.

9. Yu, H.; Sanchez-Rodriguez, J. A.; Pollum, M.; Crespo-Hernandez, C. E.; Mai, S.; Marquetand, P.; Gonzalez, L.; Ullrich, S., Internal Conversion and Intersystem Crossing Pathways in UV Excited, Isolated Uracils and Their Implications in Prebiotic Chemistry. *Phys. Chem. Chem. Phys.* **2016,** *18* (30), 20168-20176, DOI: 10.1039/c6cp01790h.

10. Boldissar, S.; de Vries, M. S., How Nature Covers Its Bases. *Phys. Chem. Chem. Phys.* **2018,** *20* (15), 9701-9716, DOI: 10.1039/c8cp01236a.

11. Buchner, F.; Nakayama, A.; Yamazaki, S.; Ritze, H. H.; Lübcke, A., Excited-State Relaxation of Hydrated Thymine and Thymidine Measured by Liquid-Jet Photoelectron Spectroscopy: Experiment and Simulation. *J. Am. Chem. Soc.* **2015,** *137* (8), 2931-2938, DOI: 10.1021/ja511108u.

12. Buchner, F. Time-Resolved Photoelectron Spectroscopy of DNA Molecules in Solution. Ph. D. Thesis, Free University Berlin, 2015.

13. Erickson, B. A.; Heim, Z. N.; Pieri, E.; Liu, E.; Martinez, T. J.; Neumark, D. M., Relaxation Dynamics of Hydrated Thymine, Thymidine, and Thymidine Monophosphate Probed by Liquid Jet Time-Resolved Photoelectron Spectroscopy. *J. Phys. Chem. A* **2019,** *123* (50), 10676-10684, DOI: 10.1021/acs.jpca.9b08258.

14. Ma, C. S.; Cheng, C. C. W.; Chan, C. T. L.; Chan, R. C. T.; Kwok, W. M., Remarkable Effects of Solvent

and Substitution on the Photo-Dynamics of Cytosine: a Femtosecond Broadband Time-Resolved Fluorescence and Transient Absorption Study. *Phys. Chem. Chem. Phys.* **2015,** *17* (29), 19045-19057, DOI: 10.1039/c5cp02624e.

15. Wang, X. L.; Zhou, Z. N.; Tang, Y. K.; Chen, J. Q.; Zhong, D. P.; Xu, J. H., Excited State Decay Pathways of 2 '-Deoxy-5-methylcytidine and Deoxycytidine Revisited in Solution: A Comprehensive Kinetic Study by Femtosecond Transient Absorption. *J. Phys. Chem. B* **2018,** *122* (28), 7027-7037, DOI: 10.1021/acs.jpcb.8b00927.

16. Milovanovic, B.; Novak, J.; Etinski, M.; Domcke, W.; Doslic, N., Simulation of UV Absorption Spectra and Relaxation Dynamics of Uracil and Uracil-Water Clusters. *Phys. Chem. Chem. Phys.* **2021,** *23* (4), 2594-2604, DOI: 10.1039/d0cp05618a.

17. Szabla, R.; Kruse, H.; Sponer, J.; Gora, R. W., Water-Chromophore Electron Transfer Determines the Photochemistry of Cytosine and Cytidine. *Phys. Chem. Chem. Phys.* **2017,** *19* (27), 17531-17537, DOI: 10.1039/c7cp02635h.

18. Borrego-Varillas, R.; Nenov, A.; Kabacinski, P.; Conti, I.; Ganzer, L.; Oriana, A.; Jaiswal, V. K.; Delfino, I.; Weingart, O.; Manzoni, C.; Rivalta, I.; Garavelli, M.; Cerullo, G., Tracking Excited State Decay Mechanisms of Pyrimidine Nucleosides in Real Time. *Nat. Commun.* **2021,** *12* (1), 7285, DOI: 10.1038/s41467-021-27535-7.

19. De Camillis, S.; Miles, J.; Alexander, G.; Ghafur, O.; Williams, I. D.; Townsend, D.; Greenwood, J. B., Ultrafast Non-Radiative Decay of Gas-Phase Nucleosides. *Phys. Chem. Chem. Phys.* **2015,** *17* (36), 23643-23650, DOI: 10.1039/c5cp03806e.

20. Yu, C.; Odonnell, T. J.; Lebreton, P. R., Ultraviolet Photo-Electron Studies of Volatile Nucleoside Models - Vertical Ionization-Potential Measurements of Methylated Uridine, Thymidine, Cytidine, and Adenosine. *J. Phys. Chem.* **1981,** *85* (25), 3851-3855, DOI: 10.1021/j150625a028.

21. Mai, S.; Marquetand, P.; Richter, M.; Gonzalez-Vazquez, J.; Gonzalez, L., Singlet and Triplet Excited-State Dynamics Study of the Keto and Enol Tautomers of Cytosine. *ChemPhysChem* **2013,** *14* (13), 2920-2931, DOI: 10.1002/cphc.201300370.

22. Ho, J. W.; Yen, H. C.; Chou, W. K.; Weng, C. N.; Cheng, L. H.; Shi, H. Q.; Lai, S. H.; Cheng, P. Y., Disentangling Intrinsic Ultrafast Excited-State Dynamics of Cytosine Tautomers. *J. Phys. Chem. A* **2011,** *115* (30), 8406-8418, DOI: 10.1021/jp205603w.

23. Wei, S. C.; Ho, J. W.; Yen, H. C.; Shi, H. Q.; Cheng, L. H.; Weng, C. N.; Chou, W. K.; Chiu, C. C.; Cheng, P. Y., Ultrafast Excited-State Dynamics of Hydrogen-Bonded Cytosine Microsolvated Clusters with Protic and Aprotic Polar Solvents. *J. Phys. Chem. A* **2018,** *122* (49), 9412-9425, DOI: 10.1021/acs.jpca.8b09526.

24. Sapunar, M.; Domcke, W.; Doslic, N., UV Absorption Spectra of DNA Bases in the 350-190 nm Range: Assignment and State Specific Analysis of Solvation Effects. *Phys. Chem. Chem. Phys.* **2019,** *21* (41), 22782-22793, DOI: 10.1039/c9cp04662c.

25. Chakraborty, P.; Liu, Y. S.; McClung, S.; Weinacht, T.; Matsika, S., Time Resolved Photoelectron Spectroscopy as a Test of Electronic Structure and Nonadiabatic Dynamics. *J. Phys. Chem. Lett.* **2021,** *12* (21), 5099-5104, DOI: 10.1021/acs.jpclett.1c00926.

26. Wolf, T. J. A.; Parrish, R. M.; Myhre, R. H.; Martinez, T. J.; Koch, H.; Guhr, M., Observation of Ultrafast Intersystem Crossing in Thymine by Extreme Ultraviolet Time-Resolved Photoelectron Spectroscopy. *J. Phys.*

Chem. A **2019,** *123* (32), 6897-6903, DOI: 10.1021/acs.jpca.9b05573.

27. Wolf, T. J. A.; Myhre, R. H.; Cryan, J. P.; Coriani, S.; Squibb, R. J.; Battistoni, A.; Berrah, N.; Bostedt, C.; Bucksbaum, P.; Coslovich, G.; Feifel, R.; Gaffney, K. J.; Grilj, J.; Martinez, T. J.; Miyabe, S.; Moeller, S. P.; Mucke, M.; Natan, A.; Obaid, R.; Osipov, T.; Plekan, O.; Wang, S.; Koch, H.; Guhr, M., Probing Ultrafast ππ*/nπ* Internal Conversion in Organic Chromophores via K-Edge Resonant Absorption. *Nat. Commun.* **2017,** *8*, DOI: 10.1038/s41467-017-00069-7.

28. Tsuchiya, Y.; Tamura, T.; Fujii, M.; Ito, M., Keto-Enol Tautomer of Uracil and Thymine. *J. Phys. Chem.* **1988,** *92* (7), 1760-1765, DOI: 10.1021/j100318a013.

29. Luckhaus, D.; Yamamoto, Y. I.; Suzuki, T.; Signorell, R., Genuine Binding Energy of the Hydrated Electron. *Sci. Adv.* **2017,** *3* (4), DOI: 10.1126/sciadv.1603224.

30. West, C. W.; Nishitani, J.; Higashimura, C.; Suzuki, T., Extreme Ultraviolet Time-Resolved Photoelectron Spectroscopy of Aqueous Aniline Solution: Enhanced Surface Concentration and Pump-Induced Space Charge Effect. *Mol. Phys.* **2021,** *119* (1-2), DOI: 10.1080/00268976.2020.1748240.

31. Yamamoto, Y.; Ishiyama, T.; Morita, A.; Suzuki, T., Exploration of Gas-Liquid Interfaces for Liquid Water and Methanol Using Extreme Ultraviolet Laser Photoemission Spectroscopy. *J. Phys. Chem. B* **2021,** *125* (37), 10514-10526, DOI: 10.1021/acs.jpcb.1c04765.

32. Kurahashi, N.; Karashima, S.; Tang, Y.; Horio, T.; Abulimiti, B.; Suzuki, Y. I.; Ogi, Y.; Oura, M.; Suzuki, T., Photoelectron Spectroscopy of Aqueous Solutions: Streaming Potentials of NaX (X = Cl, Br, and I) Solutions and Electron Binding Energies of Liquid Water and X^-. *J. Chem. Phys.* **2014,** *140* (17), 174506, DOI: 10.1063/1.4871877.

33. Martinez-Fernandez, L.; Pepino, A. J.; Segarra-Marti, J.; Jovaisaite, J.; Vaya, I.; Nenov, A.; Markovitsi, D.; Gustavsson, T.; Banyasz, A.; Garavelli, M.; Improta, R., Photophysics of Deoxycytidine and 5-Methyldeoxycytidine in Solution: A Comprehensive Picture by Quantum Mechanical Calculations and Femtosecond Fluorescence Spectroscopy. *J. Am. Chem. Soc.* **2017,** *139* (23), 7780-7791, DOI: 10.1021/jacs.7b01145.

34. Quinn, S.; Doorley, G. W.; Watson, G. W.; Cowan, A. J.; George, M. W.; Parker, A. W.; Ronayne, K. L.; Towrie, M.; Kelly, J. M., Ultrafast IR Spectroscopy of the Short-Lived Transients Formed by UV Excitation of Cytosine Derivatives. *Chem. Commun.* **2007,** (21), 2130-2132, DOI: 10.1039/b703344c.

35. Onidas, D.; Markovitsi, D.; Marguet, S.; Sharonov, A.; Gustavsson, T., Fluorescence Properties of DNA Nucleosides and Nucleotides: A Refined Steady-State and Femtosecond Investigation. *J. Phys. Chem. B* **2002,** *106* (43), 11367-11374, DOI: 10.1021/jp026063g.

36. Schroeder, C. A.; Pluharova, E.; Seidel, R.; Schroeder, W. P.; Faubel, M.; Slavíček, P.; Winter, B.; Jungwirth, P.; Bradforth, S. E., Oxidation Half-Reaction of Aqueous Nucleosides and Nucleotides via Photoelectron Spectroscopy Augmented by ab Initio Calculations. *J. Am. Chem. Soc.* **2015,** *137* (1), 201-209, DOI: 10.1021/ja508149e.

37. Pepino, A. J.; Segarra-Marti, J.; Nenov, A.; Rivalta, I.; Improta, R.; Garavelli, M., UV-Induced Long-Lived Decays in Solvated Pyrimidine Nucleosides Resolved at the MS-CASPT2/MM Level. *Phys. Chem. Chem. Phys.* **2018,** *20* (10), 6877-6890, DOI: 10.1039/c7cp08235e.

38. Gustavsson, T.; Banyasz, A.; Lazzarotto, E.; Markovitsi, D.; Scalmani, G.; Frisch, M. J.; Barone, V.; Improta, R., Singlet Excited-State Behavior of Uracil and Thymine in Aqueous Solution: A Combined Experimental and Computational Study of 11 Uracil Derivatives. *J. Am. Chem. Soc.* **2006,** *128* (2), 607-619, DOI: 10.1021/ja056181s.

39. Xue, B.; Yabushita, A.; Kobayashi, T., Ultrafast Dynamics of Uracil and Thymine Studied Using a Sub-10 fs Deep Ultraviolet Laser. *Phys. Chem. Chem. Phys.* **2016,** *18* (25), 17044-17053, DOI: 10.1039/c5cp07861j.

40. Milovanovic, B.; Kojic, M.; Petkovic, M.; Etinski, M., New Insight into Uracil Stacking in Water from ab Initio Molecular Dynamics. *J. Chem. Theory Comput.* **2018,** *14* (5), 2621-2632, DOI: 10.1021/acs.jctc.8b00139.

41. Majdi, Y.; Hochlaf, M.; Pan, Y.; Lau, K. C.; Poisson, L.; Garcia, G. A.; Nahon, L.; Al-Mogren, M. M.; Schwell, M., Theoretical and Experimental Photoelectron Spectroscopy Characterization of the Ground State of Thymine Cation. *J. Phys. Chem. A* **2015,** *119* (23), 5951-5958, DOI: 10.1021/jp510716c.

42. Majer, K.; Signorell, R.; Heringa, M. F.; Goldmann, M.; Hemberger, P.; Bodi, A., Valence Photoionization of Thymine: Ionization Energies, Vibrational Structure, and Fragmentation Pathways from the Slow to the Ultrafast. *Chem. Eur. J.* **2019,** *25* (62), 14192-14204, DOI: 10.1002/chem.201903282.

43. Choi, K. W.; Lee, J. H.; Kim, S. K., Ionization Spectroscopy of a DNA Base: Vacuum-Ultraviolet Mass-Analyzed Threshold Ionization Spectroscopy of Jet-Cooled Thymine. *J. Am. Chem. Soc.* **2005,** *127* (45), 15674-15675, DOI: 10.1021/ja055018u.

44. Hochlaf, M.; Pan, Y.; Lau, K. C.; Majdi, Y.; Poisson, L.; Garcia, G. A.; Nahon, L.; Al Mogren, M. M.; Schwell, M., Vibrationally Resolved Photoelectron Spectroscopy of Electronic Excited States of DNA Bases: Application to the Ã State of Thymine Cation. *J. Phys. Chem. A* **2015,** *119* (7), 1146-53, DOI: 10.1021/acs.jpca.5b00466.

45. Shao, Y.; Gan, Z.; Epifanovsky, E.; Gilbert, A. T. B.; Wormit, M.; Kussmann, J.; Lange, A. W.; Behn, A.; Deng, J.; Feng, X.; Ghosh, D.; Goldey, M.; Horn, P. R.; Jacobson, L. D.; Kaliman, I.; Khaliullin, R. Z.; Kuś, T.; Landau, A.; Liu, J.; Proynov, E. I.; Rhee, Y. M.; Richard, R. M.; Rohrdanz, M. A.; Steele, R. P.; Sundstrom, E. J.; Woodcock, H. L.; Zimmerman, P. M.; Zuev, D.; Albrecht, B.; Alguire, E.; Austin, B.; Beran, G. J. O.; Bernard, Y. A.; Berquist, E.; Brandhorst, K.; Bravaya, K. B.; Brown, S. T.; Casanova, D.; Chang, C.-M.; Chen, Y.; Chien, S. H.; Closser, K. D.; Crittenden, D. L.; Diedenhofen, M.; DiStasio, R. A.; Do, H.; Dutoi, A. D.; Edgar, R. G.; Fatehi, S.; Fusti-Molnar, L.; Ghysels, A.; Golubeva-Zadorozhnaya, A.; Gomes, J.; Hanson-Heine, M. W. D.; Harbach, P. H. P.; Hauser, A. W.; Hohenstein, E. G.; Holden, Z. C.; Jagau, T.-C.; Ji, H.; Kaduk, B.; Khistyaev, K.; Kim, J.; Kim, J.; King, R. A.; Klunzinger, P.; Kosenkov, D.; Kowalczyk, T.; Krauter, C. M.; Lao, K. U.; Laurent, A. D.; Lawler, K. V.; Levchenko, S. V.; Lin, C. Y.; Liu, F.; Livshits, E.; Lochan, R. C.; Luenser, A.; Manohar, P.; Manzer, S. F.; Mao, S.-P.; Mardirossian, N.; Marenich, A. V.; Maurer, S. A.; Mayhall, N. J.; Neuscamman, E.; Oana, C. M.; Olivares-Amaya, R.; O'Neill, D. P.; Parkhill, J. A.; Perrine, T. M.; Peverati, R.; Prociuk, A.; Rehn, D. R.; Rosta, E.; Russ, N. J.; Sharada, S. M.; Sharma, S.; Small, D. W.; Sodt, A.; Stein, T.; Stück, D.; Su, Y.-C.; Thom, A. J. W.; Tsuchimochi, T.; Vanovschi, V.; Vogt, L.; Vydrov, O.; Wang, T.; Watson, M. A.; Wenzel, J.; White, A.; Williams, C. F.; Yang, J.; Yeganeh, S.; Yost, S. R.; You, Z.-Q.; Zhang, I. Y.; Zhang, X.; Zhao, Y.; Brooks, B. R.; Chan, G. K. L.; Chipman, D. M.; Cramer, C. J.; Goddard, W. A.; Gordon, M. S.; Hehre, W. J.; Klamt, A.; Schaefer, H. F.; Schmidt, M. W.; Sherrill, C. D.; Truhlar, D. G.; Warshel, A.; Xu, X.; Aspuru-Guzik, A.; Baer, R.;

Bell, A. T.; Besley, N. A.; Chai, J.-D.; Dreuw, A.; Dunietz, B. D.; Furlani, T. R.; Gwaltney, S. R.; Hsu, C.-P.; Jung, Y.; Kong, J.; Lambrecht, D. S.; Liang, W.; Ochsenfeld, C.; Rassolov, V. A.; Slipchenko, L. V.; Subotnik, J. E.; Van Voorhis, T.; Herbert, J. M.; Krylov, A. I.; Gill, P. M. W.; Head-Gordon, M., Advances in Molecular Quantum Chemistry Contained in the Q-Chem 4 Program Package. *Mol. Phys.* **2015,** *113* (2), 184-215, DOI: 10.1080/00268976.2014.952696.

46. Park, W.; Lee, S.; Huix-Rotllant, M.; Filatov, M.; Choi, C. H., Impact of the Dynamic Electron Correlation on the Unusually Long Excited-State Lifetime of Thymine. *J. Phys. Chem. Lett.* **2021,** *12* (18), 4339-4346, DOI: 10.1021/acs.jpclett.1c00712.

47. Matsika, S., Electronic Structure Methods for the Description of Nonadiabatic Effects and Conical Intersections. *Chem. Rev.* **2021,** *121* (15), 9407-9449, DOI: 10.1021/acs.chemrev.1c00074.

48. Park, W.; Gulak, M. F.; Sadiq, S.; Gerasimov, I.; Lee, S. H.; Joo, T.; Choi, C. H., A Plausible Mechanism of Uracil Photohydration Involves an Unusual Intermediate. *J. Phys. Chem. Lett.* **2022**, DOI: 10.1021/acs.jpclett.2c01694.

49. Kovalenko, S. A.; Schanz, R.; Hennig, H.; Ernsting, N. P., Cooling dynamics of an optically excited molecular probe in solution from femtosecond broadband transient absorption spectroscopy. *J. Chem. Phys.* **2001,** *115* (7), 3256-3273, DOI: 10.1063/1.1380696.

50. Santoro, F.; Barone, V.; Gustavsson, T.; Improta, R., Solvent Effect on the Singlet Excited-State Lifetimes of Nucleic Acid Bases: A Computational Study of 5-Fluorouracil and Uracil in Acetonitrile and Water. *J. Am. Chem. Soc.* **2006,** *128* (50), 16312-16322, DOI: 10.1021/ja0657861.

51. Karashima, S.; Humaniuk, A.; Glover, W. J.; Suzuki, T., Ultrafast Photoisomerization of Ethylene Studied Using Time-Resolved Extreme Ultraviolet Photoelectron Spectroscopy. *J. Phys. Chem. A* **2022,** *126*, 3873-3879, DOI: 10.1021/acs.jpca.2c02468.

52. Yamazaki, S.; Taketsugu, T., Nonradiative Deactivation Mechanisms of Uracil, Thymine, and 5-Fluorouracil: A Comparative ab Initio Study. *J. Phys. Chem. A* **2012,** *116* (1), 491-503, DOI: 10.1021/jp206546g.

53. Cohen, B.; Crespo-Hernandez, C. E.; Kohler, B., Strickler-Berg Analysis of Excited Singlet State Dynamics in DNA and RNA Nucleosides. *Faraday Discuss.* **2004,** *127*, 137-147, DOI: 10.1039/b316939a.

54. Brister, M. M.; Crespo-Hernandez, C. E., Excited-State Dynamics in the RNA Nucleotide Uridine 5 '-Monophosphate Investigated Using Femtosecond Broadband Transient Absorption Spectroscopy. *J. Phys. Chem. Lett.* **2019,** *10* (9), 2156-2161, DOI: 10.1021/acs.jpclett.9b00492.

Supporting Information

Formation of long-lived dark states during electronic relaxation of pyrimidine nucleobases studied using extreme ultraviolet time-resolved photoelectron spectroscopy

Yuta Miura,[1,⊥] Yo-ichi Yamamoto,[1] Shutaro Karashima,[1] Natsumi Orimo,[1] Ayano Hara,[1,†]

Kanae Fukuoka,[1,‡] Tatsuya Ishiyama,[2] and Toshinori Suzuki[1,*]

[1]*Department of Chemistry, Graduate School of Science, Kyoto University, Kitashirakawa-Oiwakecho, Sakyo-Ku, Kyoto 606-8502, JAPAN*

[2]*Department of Applied Chemistry, Graduate School of Science and Engineering, University of Toyama, Toyama 930-8555, Japan*

AUTHOR INFORMATION

Corresponding Author

***Toshinori Suzuki** − *Department of Chemistry, Graduate School of Science, Kyoto University, Kyoto 606-8502, Japan; Email: suzuki@kuchem.kyoto-u.ac.jp*

Present Addresses

⊥Nippon Steel Corporation, Nagoya Works, 5-3 Tokaimachi, Tokai City, Aichi 476-8686, Japan

†SŪKEN Publishing Co. Ltd., Tokyo Head Office, 2-3-3 Kanda-Ogawamachi, Chiyoda-ku, Tokyo 101-0052, Japan

‡KIOXIA Corporation, Yokkaichi Plant, 800 Yamanoisshiki-cho, Yokkaichi-shi, Mie 512-8550, Japan

I. Experimental details

For high-order harmonic generation, the fundamental output (800 nm (ω)) of the amplifier was converted to 2ω laser pulses in a 0.3-mm-thick β-barium borate (BBO) crystal and focused using a quartz lens or concave mirror (f=500 mm) into a small gas tube filled with Kr. A single-order harmonic was isolated using a time-preserving monochromator.[1] The full width at half maximum (FWHM) of the extreme ultraviolet (EUV) beam at the microjet was about 100-200 μm. The photon flux in the 27.9 eV pulse (10^{11} photons/sec at 10 kHz) was more than one order of magnitude smaller than that at 21.7 eV; nevertheless, the pulse energy for unattenuated 27.9 eV radiation was sufficiently high to induce space charge effects even after monochromatization using a time-preserving monochromator for liquid sample. Thus, its intensity was attenuated to 10^9 photons/sec at 10 kHz. For the gas phase experiments, unattenuated 21.7 eV pulses (10^{11} photons/sec at 1 kHz) was used.

The 267 nm pump pulses are the third harmonic (3ω) of a Ti:sapphire laser (ω), and we employed different generation procedures for them depending on the driving laser. In the case of the 1-kHz amplifier (35 fs, 800 nm, 6 mJ/pulse), the 3ω pulses were generated by four-wave mixing of the ω and 2ω pulses in filamentation propagation in Ar, as described previously.[2-3] For the 10-kHz amplifier (35 fs, 800 nm, 0.7 mJ/pulse), 3ω pulses were generated using nonlinear frequency mixing of the ω and 2ω pulses in a BBO crystal. For the Yb:KGW amplifier (90 fs, 1030 nm, 0.4 mJ/pulse), the fundamental output was frequency quadrupled using two BBO crystals to generate pulses with a wavelength of 257 nm. The optical path length of the pump pulses was controlled using a linear translation stage with a resolution of 5 nm for gas-phase experiments, and 1.7 μm for the liquid-phase experiments. Ultraviolet (UV) and EUV pulses were focused into the photoionization chamber using a concave mirror and a toroidal mirror, respectively. The cross-correlation time between the pump and probe pulses was determined to be 47±3 fs (cross-correlation trace in Figure S1) for the gas-phase experiments, and 60±2 fs (Ti:sapphire) or 100±3 fs (Yb:KGW) for the liquid-phase experiments using a coherent artifact due to non-resonant (1+1') ionization of solvent water with the UV and EUV pulses shown in Figure 2 in the main text.

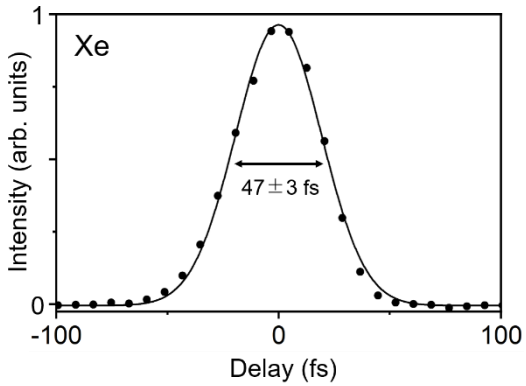

Figure S1. Non-resonant photoionization signal of Xe measured using the 267 and 57 nm pulses with the experimental setup for gas-phase experiments. Black dots are the experimental data, and a solid line is a best-fit Gaussian function.

The photoelectron kinetic energy distribution was measured using a magnetic-bottle time-of-flight electron-energy analyzer, the details of which have been previously described.[4] The analyzer was calibrated using EUV and UV photoelectron spectroscopy of gaseous Xe, CS_2 and NO. The probe photon energy was also determined from these measurements. Gaseous nucleobases were generated by heating their crystals up to about 483-493 K in a gas expansion nozzle. The mixed gas was expanded through a ⌀100 μm pinhole at a stagnation pressure of about 0.2-0.3 atm. Aqueous solutions of nucleobases were pressurized using a high-performance liquid chromatography pump and discharged from a fused silica capillary with an inner diameter of 15 μm into a photoionization chamber at a typical flow rate of 0.2 mL/min. The ionization point was about 1 mm downstream of the nozzle for both gases and liquids. The disintegrated liquid droplets were collected using a liquid nitrogen-cooled trap. Electrons were detected using a Chevron microchannel plate with a 38-mm effective diameter and a preamplifier, and electron counts were integrated using an analog-to-digital converter. The electron flight length was 1.3 m.

Samples purchased from Fujifilm Wako Pure Chemical Co. and Tokyo Chemical Industry Co. were used without further purification. The aqueous solution of cytidine (Cyd) (> 98.0% purity) was prepared with deionized solvent water (15.9 MΩ·cm) and 0.05 M NaCl was added to minimize the electrokinetic charging effect; the measured pH value was 7.7. All uracil (Ura) and thymine (Thy) derivatives were prepared in a phosphate buffer. The measured pH was 6.98 for Ura (0.01 M, > 99.0% purity), 6.93 for uridine (Urd) (0.15 M, > 98.0% purity), 7.48 for uridine 5'-monophosphate (UMP) (0.15 M, > 98.0 % purity), 7.02 for Thy (0.01 M, >98.0% purity), and 6.89 for thymidine (Thd) (0.15 M and 0.015 M, >98.0% purity). UMP is doubly charged and electrically balanced with the counter ions (Na^+).

II. Aqueous solution

A. Coherent artifact in pump-probe photoemission spectra

Figure S2 shows the photoemission spectra before subtraction of the coherent artifact.

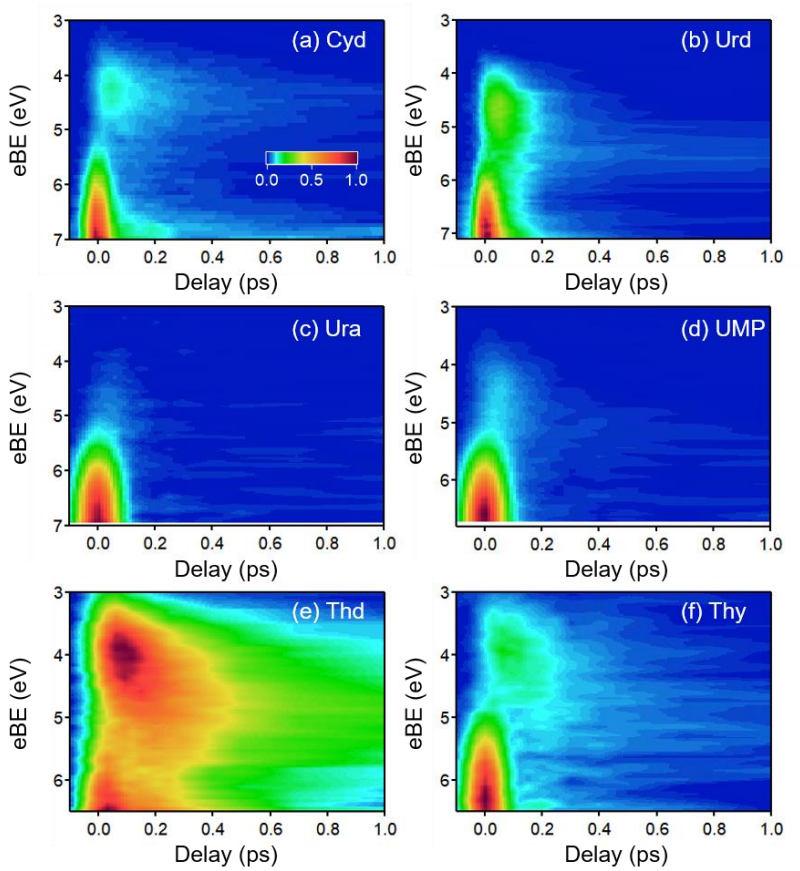

Figure S2. Pump-probe photoemission spectra for aqueous (a) 0.15 M Cyd, (b) 0.15 M Urd, (c) 0.01 M Ura, (d) 0.15 M UMP, (e) 0.15 M Thd, (f) 0.01 M Thy. The measurements of Cyd and Urd were performed with the cross-correlation time of 60 fs while those of Ura, UMP, Thd, and Thy with 100 fs. The temporal widths of the coherent artifact are different between these two types of measurements.

B. Results of Global Fitting

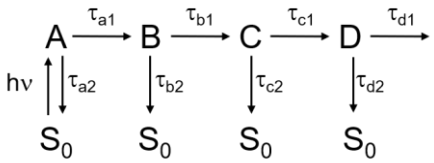

Scheme S1. Kinetic scheme employed for global fitting analysis of the spectra.

The observed spectral features clearly indicate that the spectral evolution corresponds to the electronic relaxation process $^1\pi\pi^* \rightarrow {}^1n\pi^* \rightarrow {}^3\pi\pi^*$. Thus, we performed a global fitting analysis for the spectral evolution of aqueous nucleobases. We assumed a kinetic scheme shown in Scheme S1 which explicitly includes internal conversion to S_0 state at each step. The analytical solution of the corresponding rate equations is as follows:

$$[A] = e^{-t/\tau_a} \quad \text{(S1)}$$

$$[B] = r_a\tau_b\left(\frac{e^{-t/\tau_a}}{\tau_{ab}} + \frac{e^{-t/\tau_b}}{\tau_{ba}}\right) \quad \text{(S2)}$$

$$[C] = r_a r_b\tau_c\left(\frac{\tau_a e^{-t/\tau_a}}{\tau_{ab}\tau_{ac}} + \frac{\tau_b e^{-t/\tau_b}}{\tau_{ba}\tau_{bc}} + \frac{\tau_c e^{-t/\tau_c}}{\tau_{ca}\tau_{cb}}\right) \quad \text{(S3)}$$

$$[D] = r_a r_b r_c\tau_d\left(\frac{{\tau_a}^2 e^{-t/\tau_a}}{\tau_{ab}\tau_{ac}\tau_{ad}} + \frac{{\tau_b}^2 e^{-t/\tau_b}}{\tau_{ba}\tau_{bc}\tau_{bd}} + \frac{{\tau_c}^2 e^{-t/\tau_c}}{\tau_{ca}\tau_{cb}\tau_{cd}} + \frac{{\tau_d}^2 e^{-t/\tau_d}}{\tau_{da}\tau_{db}\tau_{dc}}\right) \quad \text{(S4)}$$

where $[X]$ is the population in state X(X = A, B, C, D), $\tau_x = (\tau_{x1}^{-1} + \tau_{x2}^{-1})^{-1}(x = a, b, c, d)$ is the lifetime of state X, $\tau_{xy} = \tau_x - \tau_y\ (x, y = a, b, c, d)$, $r_x = \tau_x\tau_{x1}^{-1}(x = a, b, c)$ is the branching ratio. τ_{x2} is obtained as $\tau_x(1 - r_x)^{-1}$.

In the global fitting analysis, we broke down $[X]$ into the contribution from each energy bin, $P_X(t, E_k)$, as follows:

$$P_A(t, E_k) = c_{ak}e^{-t/\tau_a} \quad \text{(S5)}$$

$$P_B(t, E_k) = c_{bk}\tau_b\left(\frac{e^{-t/\tau_a}}{\tau_{ab}} + \frac{e^{-t/\tau_b}}{\tau_{ba}}\right) \quad \text{(S6)}$$

$$P_C(t, E_k) = c_{ck}\tau_c\left(\frac{\tau_a e^{-t/\tau_a}}{\tau_{ab}\tau_{ac}} + \frac{\tau_b e^{-t/\tau_b}}{\tau_{ba}\tau_{bc}} + \frac{\tau_c e^{-t/\tau_c}}{\tau_{ca}\tau_{cb}}\right) \quad \text{(S7)}$$

$$P_D(t, E_k) = c_{dk}\tau_d\left(\frac{{\tau_a}^2 e^{-t/\tau_a}}{\tau_{ab}\tau_{ac}\tau_{ad}} + \frac{{\tau_b}^2 e^{-t/\tau_b}}{\tau_{ba}\tau_{bc}\tau_{bd}} + \frac{{\tau_c}^2 e^{-t/\tau_c}}{\tau_{ca}\tau_{cb}\tau_{cd}} + \frac{{\tau_d}^2 e^{-t/\tau_d}}{\tau_{da}\tau_{db}\tau_{dc}}\right) \quad \text{(S8)}$$

where k is an index for equally spaced electron binding energy (eBE) bins, $c_{xk}\ (x = a, b, c, d)$ is an expansion coefficient. c_{xk} fulfills the following relation:

$$\sum_k c_{ak}\Delta E = 1 \quad \text{(S9)}$$

$$\sum_k c_{bk}\Delta E = r_a \quad \text{(S10)}$$

$$\sum_k c_{ck}\Delta E = r_a r_b \quad \text{(S11)}$$

$$\sum_k c_{dk}\Delta E = r_a r_b r_c \quad \text{(S12)}$$

where ΔE is a width of eBE bin.

The spectral evolution is expressed as:

$$I(t, E_k) = \sigma_0\{P_A(t, E_k) + P_B(t, E_k) + P_C(t, E_k) + P_D(t, E_k)\} \otimes g(t) \quad \text{(S13)}$$

where σ_0 is a photoemission cross-section that was assumed to be identical for all species, $g(t)$ is a Gaussian cross-correlation function for the laser pulses.

We employed Eq. S13 for Cyd, Thd, and Thy. For Cyd, A corresponds to $^1\pi\pi^*$ in the Franck-Condon region, B and C to $^1\pi\pi^*$ after vibrational motions, and D to $^1n\pi^*$. For Thd and Thy, A and B correspond to $^1\pi\pi^*$ in the Franck-Condon region and after vibrational motions, and C and D to $^1n\pi^*$ and $^3\pi\pi^*$, respectively.

For Urd and UMP, three components were sufficient to express the entire spectral evolution, because these molecules have an extremely short lifetime for the $^1\pi\pi^*$ state and the spectral evolution in $^1\pi\pi^*$ was not discernible. Thus, we employed the following Eq. S14 by removing the term for D.

$$I(t, E_k) = \sigma_0\{P_A(t, E_k) + P_B(t, E_k) + P_C(t, E_k)\} \otimes g(t) \quad \text{(S14)}$$

In these cases, A corresponds to $^1\pi\pi^*$, and B and C to $^1n\pi^*$ and $^3\pi\pi^*$, respectively. We employed the following Eq. S15 in the analysis of Ura by further removing the term for C, because it was difficult to distinguish the $^1n\pi^*$ and $^3\pi\pi^*$ states due to the extremely low signal level.

$$I(t, E_k) = \sigma_0\{P_A(t, E_k) + P_B(t, E_k)\} \otimes g(t) \qquad \text{(S15)}$$

The results of global fitting are shown in Figures S3, S4 and S5. The expansion coefficients in Eqs. S13, S14, and S15 provide the spectra extracted for each transient state, as shown in Figures 4(c), 5(c), (f), (i), 6(b), and (d). The best-fit results reproduce the observed spectra reasonably well, and the residuals are comparable to the noise level.

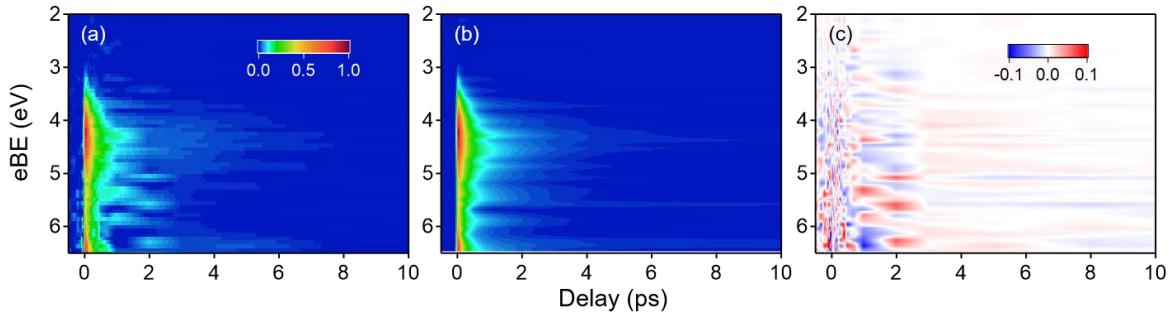

Figure S3. Results of global fitting of spectra of aqueous solution of Cyd. Photoemission spectra for (a) 0.15 M Cyd, (b) reproduced spectra for (a), (c) residuals calculated from (a) and (b).

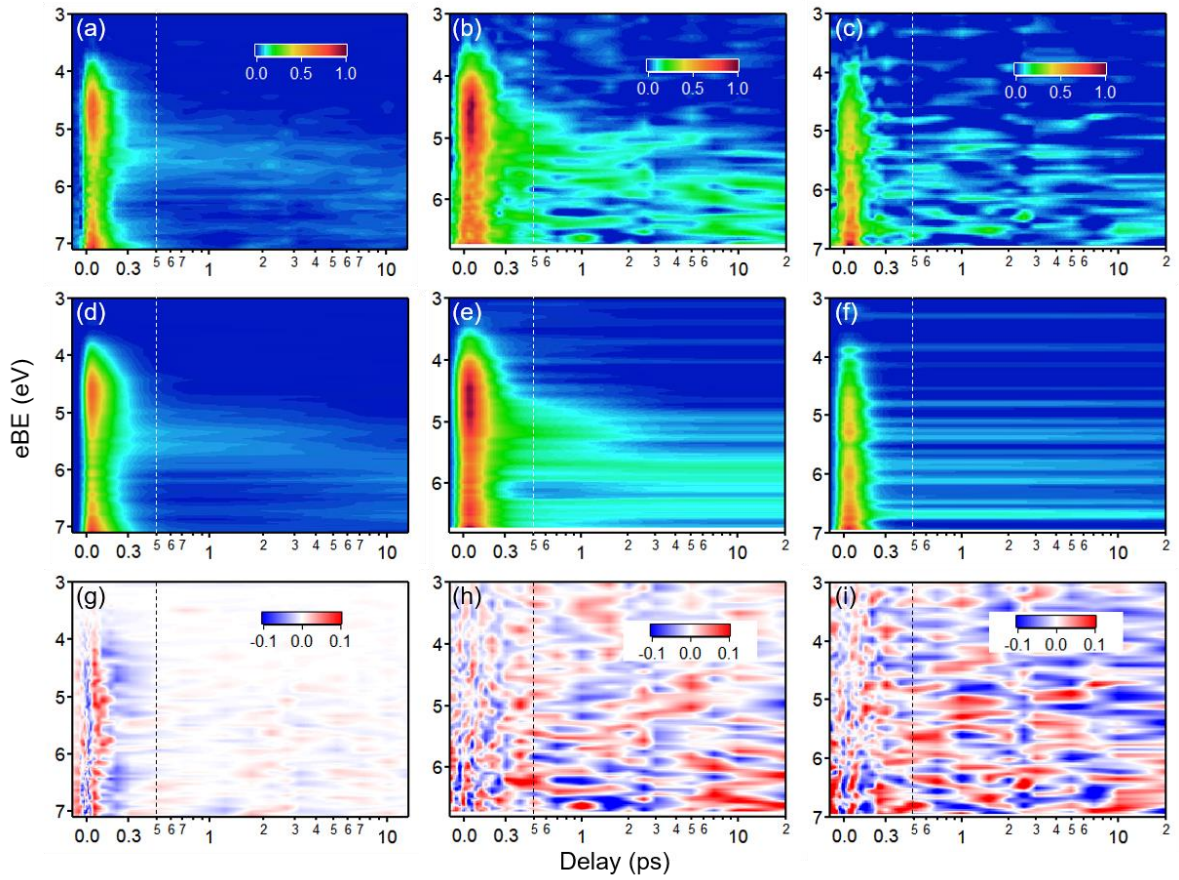

Figure S4. Results of global fitting of spectra of aqueous solution of Ura derivatives. Photoemission spectra for (a) 0.15 M Urd, (b) 0.15 M UMP, and (c) 0.01 M Ura, (d-f) reproduced spectra for (a-c), (g-i) residuals calculated from (a-c) and (d-f). Figures 5(d), (e), (g) and (h) are generated by boxcar smoothing of the data shown in (b), (c).

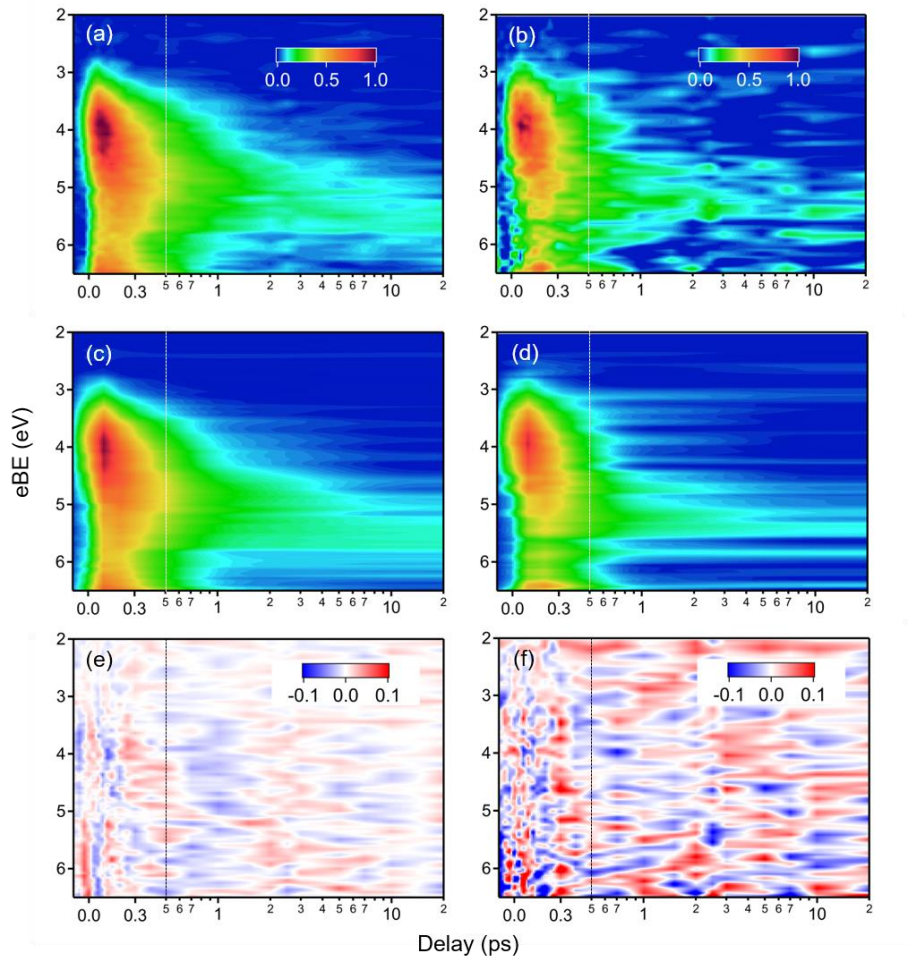

Figure S5. Results of global fitting of spectra of aqueous solution of Thy derivatives. Photoemission spectra for (a) 0.15 M Thd and (b) 0.01 M Thy. (c, d) reproduced spectra for (a, b), (e, f) residuals calculated from (a, b) and (c, d).

C. Decomposition of $^1\pi\pi^*$ and $^1n\pi^*$ spectra

In order to evaluate the quantum yield for $^1n\pi^*$, overlapping photoelectron bands in the spectra of $^1\pi\pi^*$ and $^1n\pi^*$ were decomposed into individual bands. We performed least squares fitting using two Gaussian functions or two exponentially modified Gaussian (EMG) functions. Figures S6, S7, S8, S9, S10 and S11 show the fitting results for Cyd, Urd, Ura, UMP, Thd, and Thy, respectively; in all cases, the Gauss fit results are shown in (a) and the EMG fit results in (b). As shown in Figure S7(a), least-squares fitting of the spectrum using two Gaussian functions tends to underestimate the $^1\pi\pi^*$ band intensity, providing the upper bound for an estimated $^1n\pi^*$ quantum yield (0.06). Fitting using two EMG functions provides a smaller $^1n\pi^*$ quantum yield of 0.04 as shown in Figure S7(b). EMG is defined by

$$f(eBE) = \sum_i^2 a_i \exp\left\{-\left(\frac{eBE - eBE_i}{\sqrt{2}\sigma_i}\right)^2\right\} \otimes \frac{1}{s_i}\exp\left(\frac{eBE - eBE_i}{s_i}\right) U(eBE - eBE_i)$$

$$= \sum_{i=1}^{2} a_i \sqrt{\frac{\pi}{2}} \frac{\sigma_i}{s_i} \exp\left(\frac{eBE - eBE_i}{s_i} + \frac{{\sigma_i}^2}{2{s_i}^2}\right)\left\{1 - \mathrm{erf}\left(\frac{eBE - eBE_i}{\sqrt{2}\sigma_i} + \frac{\sigma_i}{\sqrt{2}s_i}\right)\right\} \quad \text{(S16)}$$

where $U(eBE - eBE_i)$ is a step function which is unity for $eBE - eBE_i > 0$ and zero for otherwise, a_i is amplitude of the peak, σ_i is width of Gaussian, eBE_i is center of Gaussian, and s_i is inverse of rate parameter of exponential function. Thus, our best estimate of the ^{1}nπ^* quantum yield for Urd is 0.04-0.06. In the case of Cyd, the signal to noise ratio in the ^{1}nπ^* spectrum was rather low, and the least-squares fitting required some constraints. We fixed the FWHM to 1.2 eV for Gauss fit, and the shape-determining parameter σ_i and s_i to 0.41 and 0.47 eV for EMG fit, respectively. These are the same values with those determined for the $^1\pi\pi^*$ state. In the case of Ura, the signal to noise ratio in the ^{1}nπ^* spectrum is also rather low due to its low solubility. We fixed the FWHM to 1.2 eV for Gauss fit, and the shape-determining parameter σ_i and s_i to 0.64 and 0.03 eV for EMG fit, respectively, which are similar values to those for Urd and UMP.

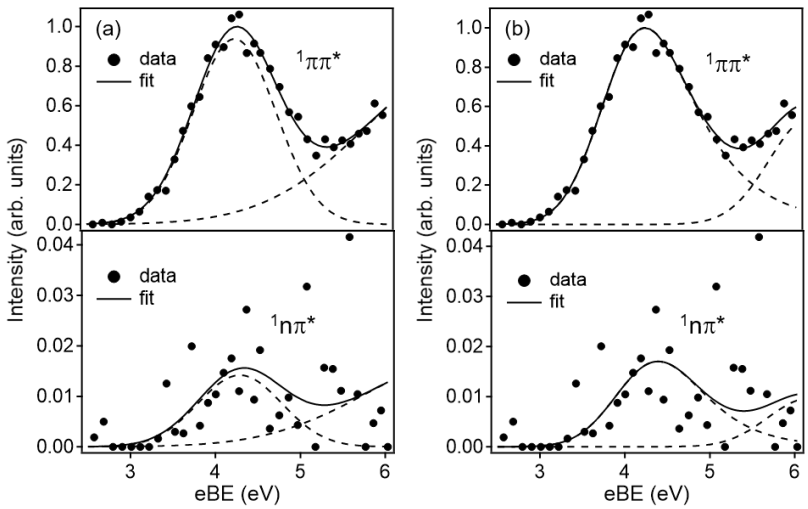

Figure S6. Decomposition of $^1\pi\pi^*$ and ^{1}nπ^* signal measured for aqueous 0.15 M Cyd with (a) two Gaussian functions and (b) two EMG functions. Solid circles indicate experimental data points. The dashed lines show individual components, and the solid line is the sum of the two components.

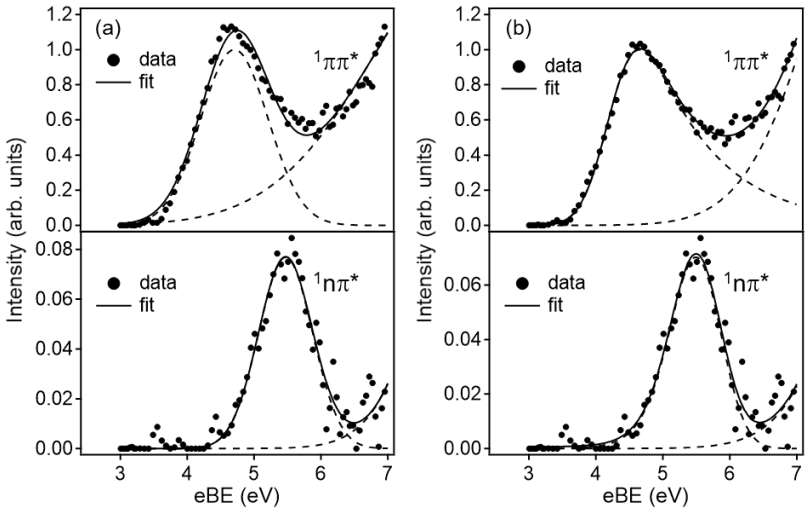

Figure S7. Decomposition of $^1\pi\pi^*$ and $^1n\pi^*$ signal measured for aqueous 0.15 M Urd with (a) two Gaussian functions and (b) two EMG functions. Solid circles indicate experimental data points. The dashed lines show individual components, and the solid line is the sum of the two components.

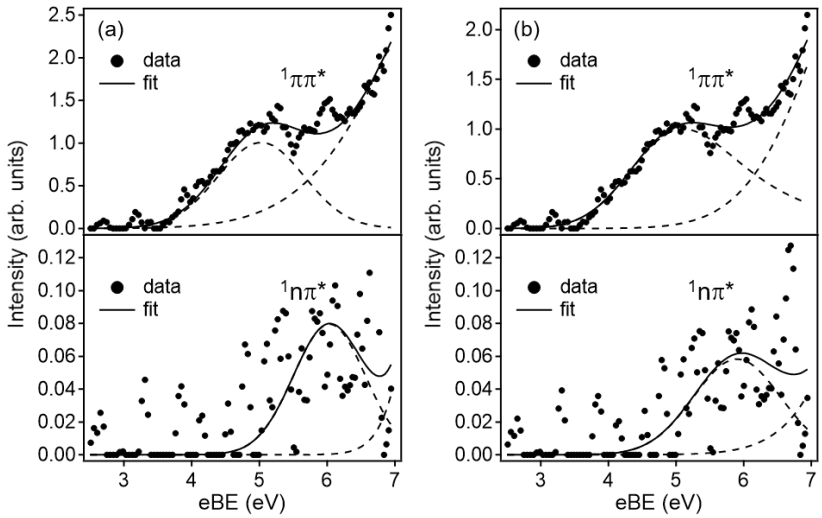

Figure S8. Decomposition of $^1\pi\pi^*$ and $^1n\pi^*$ signal measured for aqueous 0.01 M Ura with (a) two Gaussian functions and (b) two EMG functions. Solid circles indicate experimental data points. The dashed lines show individual components, and the solid line is the sum of the two components.

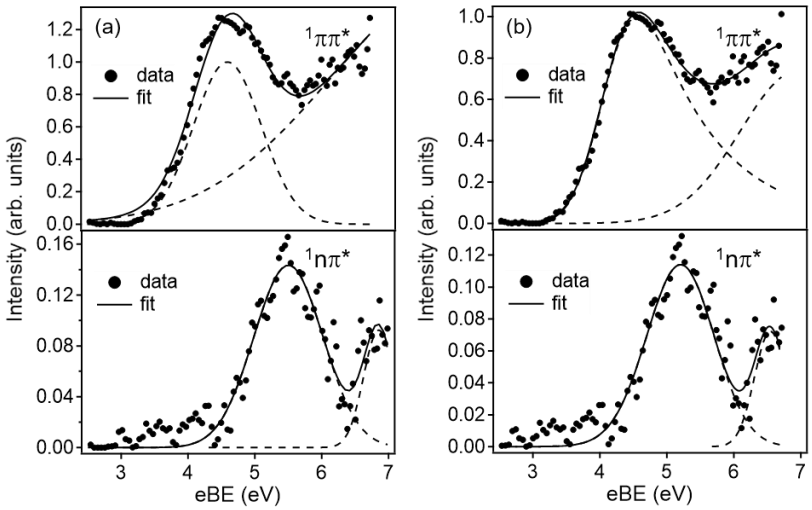

Figure S9. Decomposition of $^1\pi\pi^*$ and $^1n\pi^*$ signal measured for aqueous 0.15 M UMP with (a) two Gaussian functions and (b) two EMG functions. Solid circles indicate experimental data points. The dashed lines show individual components, and the solid line is the sum of the two components.

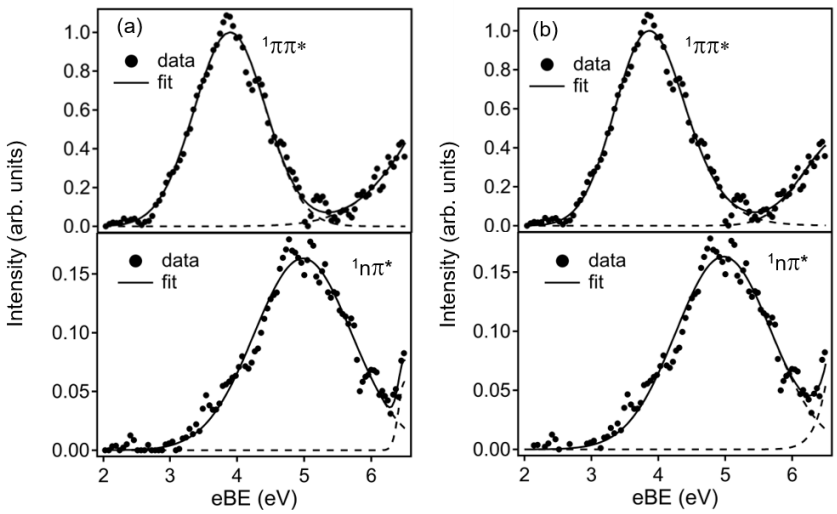

Figure S10. Decomposition of $^1\pi\pi^*$ and $^1n\pi^*$ signal measured for aqueous 0.15 M Thd with (a) two Gaussian functions and (b) two EMG functions. Solid circles indicate experimental data points. The dashed lines show individual components, and the solid line is the sum of the two components.

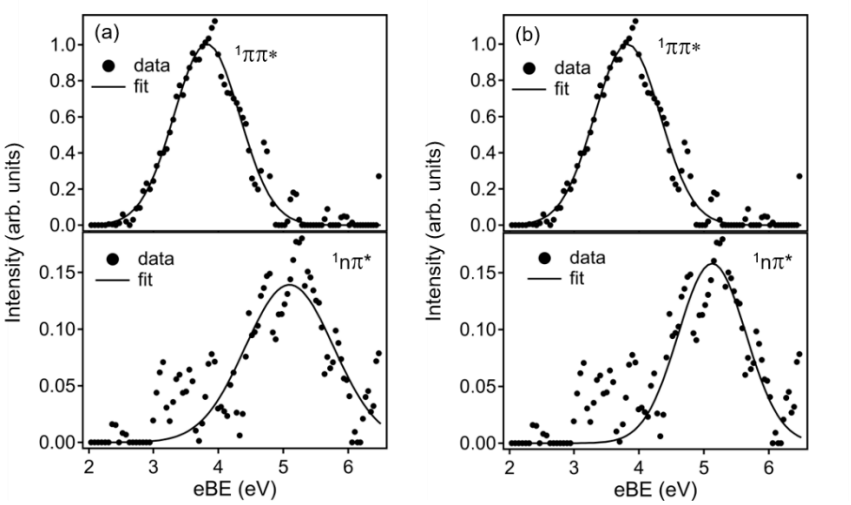

Figure S11. Decomposition of $^1\pi\pi^*$ and $^1n\pi^*$ signal measured for aqueous 0.01 M Thy with (a) Gaussian function and (b) EMG function. Solid circles indicate experimental data points. The solid line is best fitting result.

D. Simulation of bleach recovery signal observed using transient absorption spectroscopy (TAS)

In order to illustrate experimental difficulty in TAS of the ground-state bleach recovery, we performed a model calculation with the scheme shown in Figure S12(a). The results are shown in Figure S12(b). The cross-correlation time for the pump and probe pulses was assumed to be 200 fs. The cascaded electronic relaxation process shown in Figure S12(a) is expressed using the following rate equations,

$$\frac{d[P]_{FC}}{dt} = -(k_{FN} + k_{Feq} + k_{FV})[P]_{FC}$$

$$\frac{d[P]_{eq}}{dt} = k_{Feq}[P]_{FC} - k_{eqV}[P]_{eq}$$

$$\frac{d[N]}{dt} = k_{FN}[P]_{FC} - k_{NV}[N]$$

$$\frac{d[V]}{dt} = k_{FV}[P]_{FC} + k_{eqV}[P]_{eq} + k_{NV}[N] - k_{V0}[V]$$

$$\frac{d[S]_{eq}}{dt} = k_{V0}[V]$$

$$ABS = [V] * X + [S]_{eq} \quad \text{(S17)}$$

where $[P]_{FC}, [P]_{eq}, [N]$, $[V]$, and $[S]_{eq}$ are the population in the Franck-Condon region, the vibrationally randomized state in $^1\pi\pi^*$, the $^1n\pi^*$ state, the highly vibrationally excited states in S_0, and the thermally relaxed state in S_0, respectively. k_x is τ_x^{-1} $(x = FN, Feq, FV, eqV, NV, V0)$. ABS is the transient photoabsorption and stimulated emission intensity at the probe wavelength, and X $(0 \leq X \leq 1)$ is the sensitivity factor for $[V]$. Figure S12(b) shows three curves for X=0.0, 0.5 and 1.0. When highly vibrationally excited molecules in S_0 produced by internal conversion does not absorb the probe

light (X=0.0), bleach recovery occurs slowly at the vibrational relaxation time (several picoseconds), whereas if vibrationally excited molecules absorb the probe light in a similar manner to those in thermal equilibrium (X=1.0), a large fraction of the bleach recovery occurs immediately and is undetected using TAS. When this ultrafast component of bleach recovery due to direct internal conversion from $^1\pi\pi^*$ to S_0 is neglected, the quantum yield associated with direct internal conversion is underestimated, leading to overestimation of the $^1n\pi^*$ quantum yield.

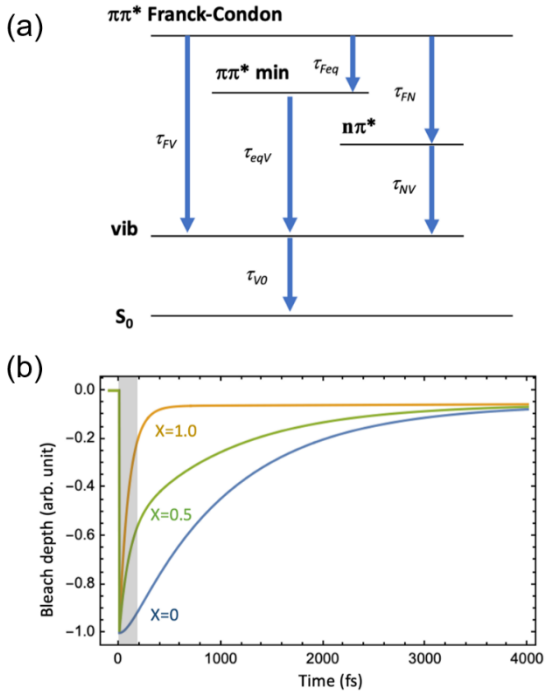

Figure S12. (a) Kinetic model for relaxation of aqueous nucleobase and (b) the results of computational simulation of the ground-state bleach recovery. The parameters are $\tau_{FV} = 0.1$ ps, $\tau_{Feq} = 0.3$ ps, $\tau_{FN} = 1.1$ ps, $\tau_{eqV} = 0.1$ ps, τ_{NV} =35.0 ps, and $\tau_{V0} = 1.0$ ps. The relaxation from the Franck-Condon region in the $^1\pi\pi^*$ state to S_0 is assumed to proceed via three pathways. The shaded region illustrates a hypothetical blind time (200 fs) of observation due to experimental disturbance such as coherent spikes. With the assumed τ_{FV}, internal conversion occurs from the $^1\pi\pi^*$ state to S_0 in this blind time range. The three curves in panel (b) illustrate how different bleach recovery is anticipated depending on the spectral overlap of hot and thermal molecules at the probe wavelength. When the overlap is 100%, the bleach recovery occurs with the time constant of τ_{FV}, while it occurs with τ_{V0} for 0%.

E. Comparison with previous studies

Table S1. Excited-state lifetimes (ps) for nucleobases in liquid phase

Molecule	Method	Pump (nm)	Probe (nm)	τ_1	τ_2	τ_3	τ_4	Year, Ref
Cyd	FU, TAS	267	416	0.24(3)	1.8(1)	35(2)		2015, 5
	TRPES	266	238	0.35				2015, 6
	FU[a, b]	267	330	0.22(1)	0.96(7)			2017, 7
	TRPES	270	44.4	0.07(1)	0.21(2)	1.3(3)	6(1)	2022, This Work
Ura	TAS	267	250		1.9(1)	24(2)		2007, 8
	TAS	270	260-285	0.054-0.128	0.11-1.64			2016, 9
	FU[a]	267	330	0.096(3)				2017, 10
	TRPES	258	46.8	0.067(3)		>20[c]		2022, This work
Urd	TAS	263	570, 600, 630	0.21				2004, 11
	TAS	275	650-270	0.097	0.48			2021, 12
	TRPES	270	46.8	0.12(2)	5(1)			2022, This work
UMP	TAS	267	250		2.3(2)	147(7)		2007, 8
	TAS	267	345-700	0.20(5)	0.43(5)	365(20)		2019, 13
	TRPES	258	46.8	0.095(3)	1.2(2)	>20[c]		2022, This work
Thy	TAS	267	250		2.8(4)	30(13)		2007, 8
	TRPES	266	238	0.07(1)	0.41(4)			2015, 14
	TAS	270	260-285	0.068-0.151	0.13-2.21			2016, 9
	FU[a]	267	330	0.20(2)	0.63(2)			2017, 10
	TRPES	261.5	200	0.36(6)				2019, 15
	TRPES	258	46.8	0.15(9)	0.16(9)	2.5(8)	>20[c]	2022, This work
Thd	TRPES	266	238	0.12(1)	0.39(1)			2015, 14
	TRPES	261.5	200	0.39(7)				2019, 15
	TAS	275	650-270	0.10				2021, 12
	TRPES	258	46.8	0.087(3)	0.25(1)	3.1(2)	>20[c]	2022, This work

[a]fluorescence up-conversion.

[b]deoxycytidine

[c]too long to be determined by the limited measurement time window.

F. Molecular dynamics (MD) simulations

We employed the SPC/E model[16] for water, the general AMBER force field (GAFF)[17] for Ura, Urd, and UMP, with partial charges set to fit the electrostatic potential generated at the B3LYP/6-31G(d,p) level using the RESP model,[18] and a force field model for ions that is compatible with the SPC/E model.[19] Initial configurations were prepared in the following way: a rectangular simulation box, which contains water and solute molecules (the number of molecules contained in the box is shown in the inset of the figure for each number density profile) as a slab geometry with the interface parallel to the *x*-*y* plane. The simulation box dimensions $L_x \times L_y \times L_z$ were set to 40 Å × 40 Å × 250 Å. Initially, water and solute molecules were placed in random positions and orientations in the central region of the cell (see Figure S13) using the PACKMOL package.[20] The steepest descent method was carried out to remove initial overlap of molecules. Newton's equation of motion was solved using the leapfrog algorithm[21] with a time step of $\Delta t = 2.0$ fs with three-dimensional periodic boundary conditions, where the bonds to H were constrained using the LINCS algorithm.[22] In the equilibration step, an NVT (constant volume and temperature) ensemble simulation was carried out, where the system temperature was kept at $T = 298.15$ K using a Nose-Hoover thermostat.[23-24] The long-range Coulombic interaction was treated using the particle-mesh Ewald method.[25-26] The cutoff distance for the Lennard-Jones potential and the real-space part of the Ewald sum were taken to be 10 Å. By checking the time evolution of averaged profiles, it was found that the MD system needed at least a 40-ns equilibration run to reach a steady equilibrium state. The subsequent 10 ns production run was conducted with 32 parallel computations starting with different initial configurations, and hence a total ensemble average was taken for 320 ns. The Gromacs package (version 5.1.2)[27] was employed for the trajectory calculation.

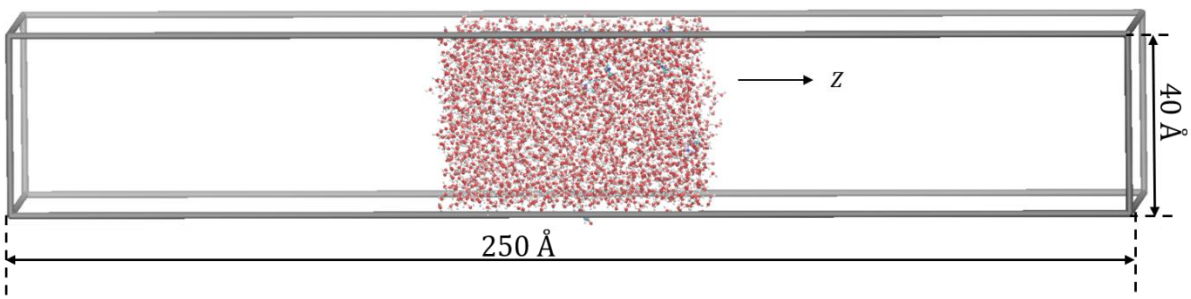

Figure S13. Snapshots of configuration after equilibration of solution in MD simulation, where 3000 water and 8 Ura molecules are considered.

The surface potential $\Delta\phi$ was calculated using:

$$\Delta\phi = \phi(z_1) - \phi(z_0) = -\int_{z_0}^{z_1} dz'\, E_z(z') \qquad \text{(S18)}$$

$$E_z(z') = \frac{1}{\varepsilon_0}\int_{z_0}^{z} dz'\,\rho_q(z') \qquad \text{(S19)}$$

where $E_z(z)$ and $\rho_q(z)$ are the normal component of the electric field and the charge density at z, and ε_0 is the dielectric permittivity of free space.

Liquid water (3000 water molecules)

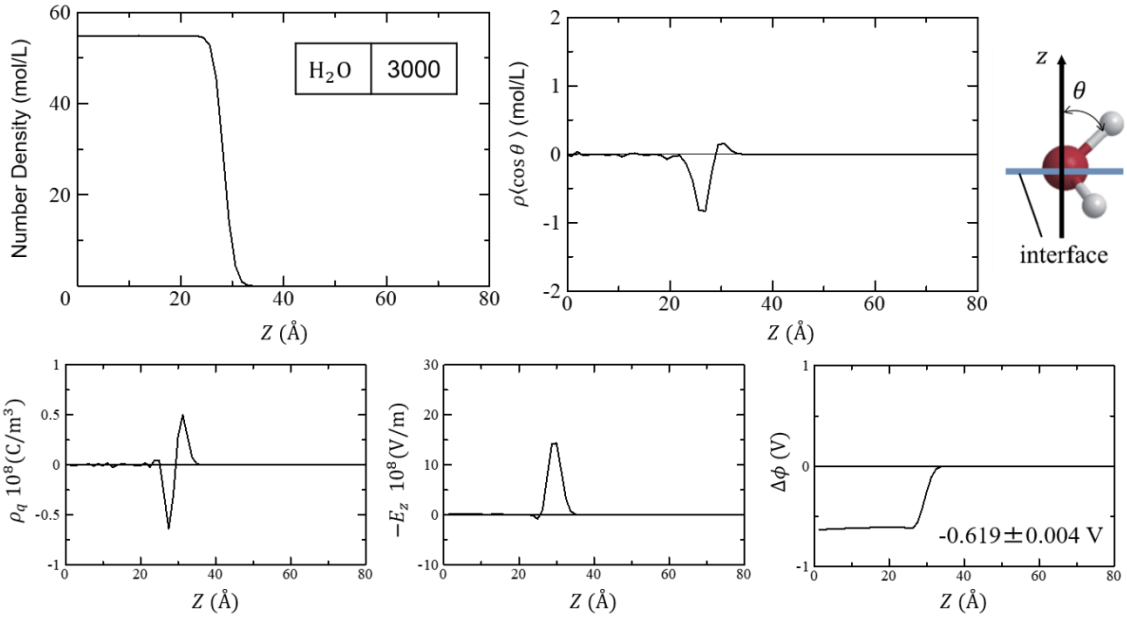

Figure S14. Upper left panel: number density (depth) profiles $\rho(z)$ for water oxygen (OW). The inset shows the number of water molecules contained in the MD system. Upper right panel: $\rho\langle cos\theta\rangle$ profiles, where ρ is the number density for water molecules and $\langle cos\theta\rangle$ is the average direction cosine (θ is the angle between the OH bond and the surface normal unit vector, as schematically shown in the figure). Lower left panel: charge density distribution $\rho_q(z)$. Lower middle panel: normal component of electric field at z, $E_z(z)$ calculated using Eq. S19. Lower right panel: difference in electric potential $\Delta\phi$ calculated using Eq. S18 where the numerical value indicates the estimated surface potential.

Aqueous Ura solution

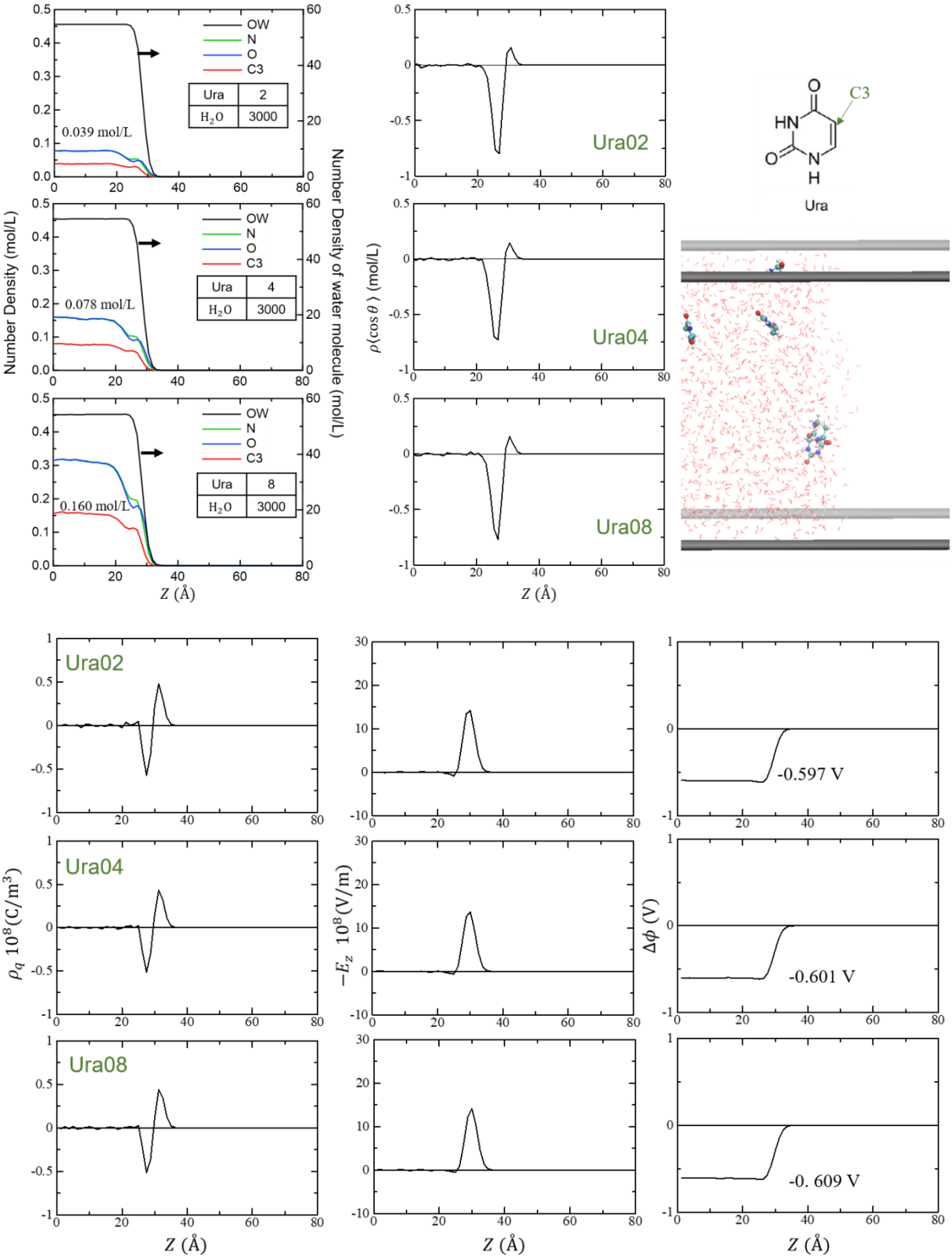

Figure S15. MD simulation results for aqueous Ura solution. Upper left panel: number density (depth) profiles $\rho(z)$ for water oxygen (OW), nitrogen (N), oxygen (O), and carbon (C3) atoms in pyrimidine rings in solutes. The inset shows the number of molecules contained in each MD system. The numerical

value in each figure indicates the average bulk number density. Upper middle panel: $\rho\langle cos\theta\rangle$ profiles computed for each aqueous solution, where ρ is the number density for water molecules, and $\langle cos\theta\rangle$ is the average direction cosine (θ is the angle between the OH bond and the surface normal unit vector). Upper right panel: Molecular structure of Ura and snapshot of MD simulation for four Ura and 3000 water molecules. Gray horizontal lines represent the boundaries of the simulation box. Lower left panel: charge density distribution $\rho_q(z)$ for each system. Lower middle panel: normal component of electric field at z, $E_z(z)$, for each system calculated using Eq. S19. Lower right panel: difference in electric potential $\Delta\phi$ for each system calculated using Eq. S18, where the numerical value in each figure indicates the estimated surface potential.

Aqueous Urd solution

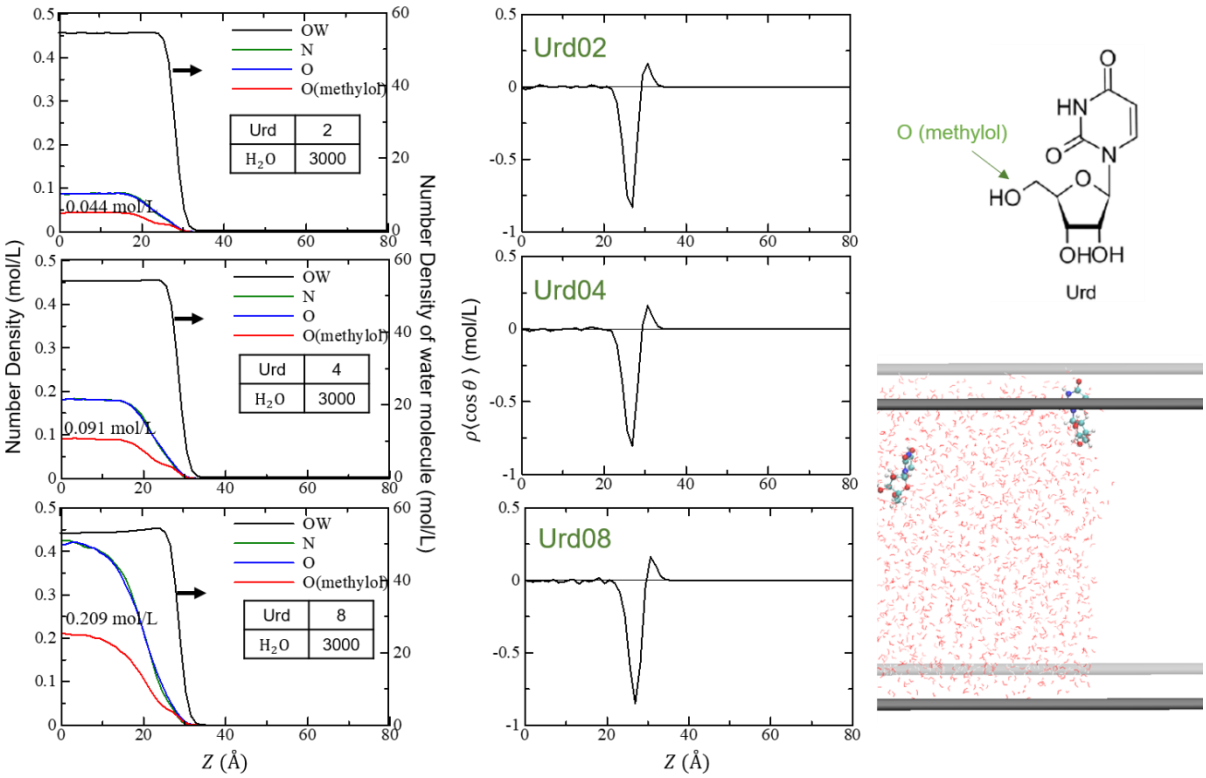

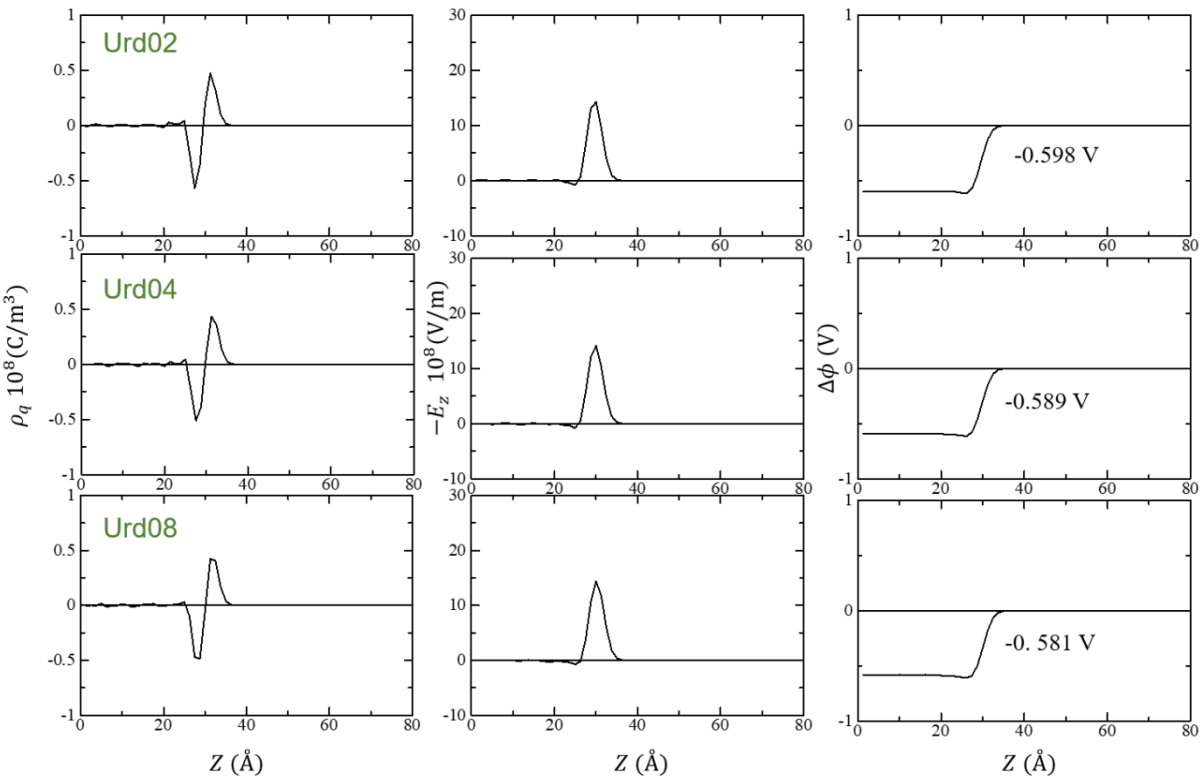

Figure S16. MD simulation results for aqueous Urd solution. Upper left panel: number density (depth) profiles $\rho(z)$ for water oxygen (OW), nitrogen (N) and oxygen (O) atoms in pyrimidine rings, and oxygen in methylol in solutes. The inset shows the number of molecules contained in each MD system. The numerical value in each figure indicates the average bulk number density. Upper middle panel: $\rho\langle cos\theta\rangle$ profile computed for each aqueous solution, where ρ is the number density for water molecules and $\langle cos\theta\rangle$ is the average direction cosine (θ is the angle between the OH bond and the surface normal unit vector). Upper right panel: Molecular structure of Urd and snapshot of MD simulation for two Urd and 3000 water molecules. Gray horizontal lines represent the boundaries of the simulation box. Lower left panel: charge density distribution $\rho_q(z)$ for each system. Lower middle panel: normal component of electric field at z, $E_z(z)$, for each system calculated using Eq. S19. Lower right panel: difference in electric potential $\Delta\phi$ for each system calculated using Eq. S18, where the numerical value in each figure indicates the estimated surface potential.

Aqueous UMP solution

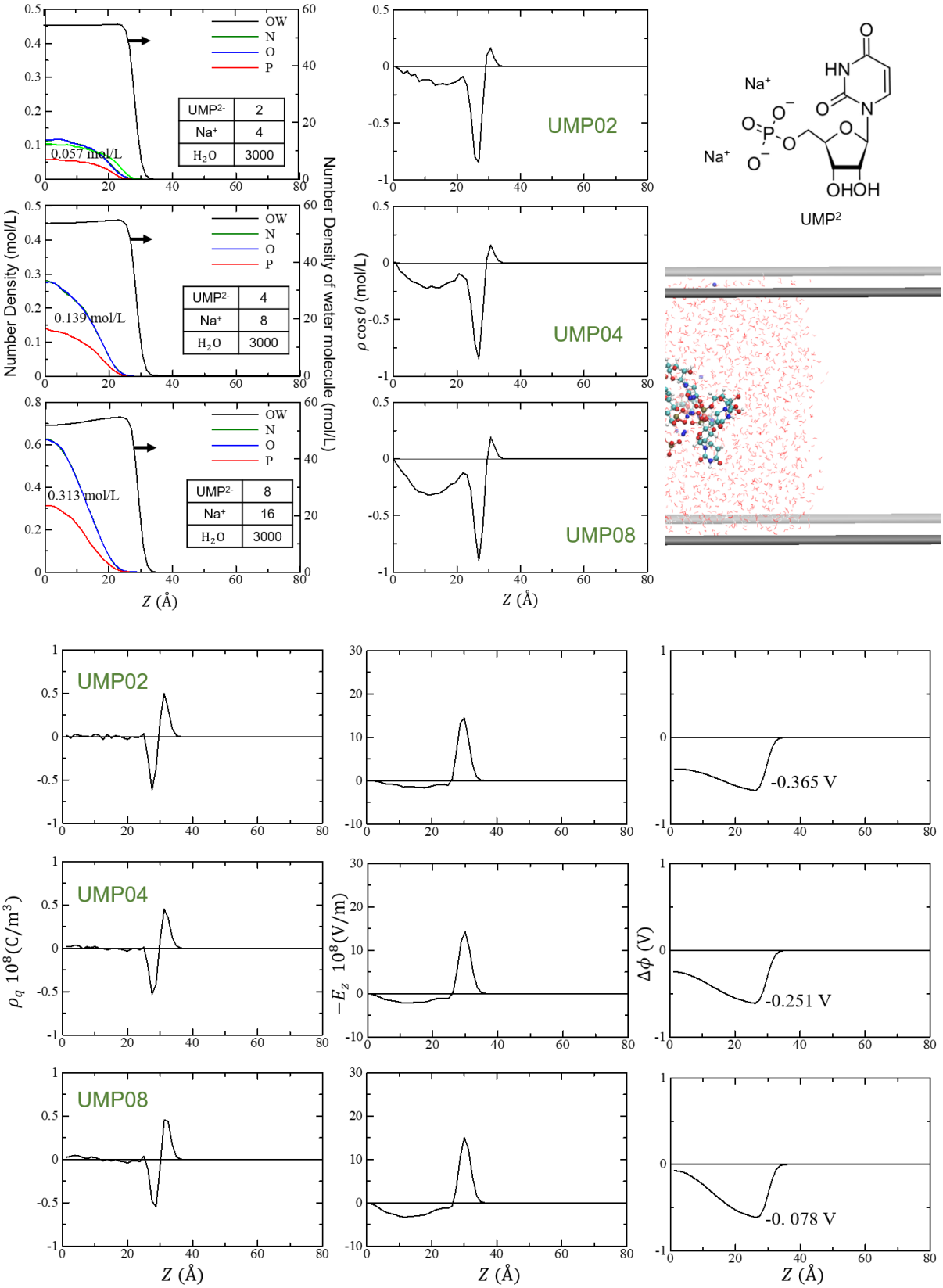

Figure S17. MD simulation results for aqueous UMP solution. Note that UMP is doubly charged and

two Na^+ per one UMP are added for charge balancing. Upper left panel: number density (depth) profiles $\rho(z)$ for water oxygen (OW), nitrogen (N) and oxygen (O) atoms in pyrimidine rings, and phosphorus (P) in solutes. The inset shows the number of molecules contained in each MD system. The numerical value in each figure indicates the average bulk number density. Upper middle panel: $\rho\langle cos\theta\rangle$ profiles computed for each aqueous solution, where ρ is the number density for water molecules and $\langle cos\theta\rangle$ is the average direction cosine (θ is the angle between the OH bond and the surface normal unit vector). Upper right panel: Molecular structure of UMP and snapshot of MD simulation for eight UMP and 3000 water molecules. Gray horizontal lines represent the boundaries of the simulation box. Lower left panel: charge density distribution $\rho_q(z)$ for each system. Lower middle panel: normal component of electric field at z, $E_z(z)$, for each system calculated using Eq. S19. Lower right panel: difference in electric potential $\Delta\phi$ for each system calculated using Eq. S18, where the numerical value in each figure indicates the estimated surface potential.

III. Gas Phase

A. Least-squares fitting of photoelectron intensity time profiles

The photoelectron signal upon ionization from $^1\pi\pi^*$ to the lowest cationic state (π^{-1}) appears in the eBE region of 3.6-5.2 eV for gaseous Thy and 4.0-5.4 eV for gaseous Ura, as shown in Figures 7(c) and 7(d) in the main text. We performed least-squares fitting of the profiles using the following functions:

$$[A] = e^{-t/\tau_a} \quad \text{(S20)}$$

$$[B] = \left(1 - e^{-t/\tau_a}\right) \quad \text{(S21)}$$

$$I(t) = (c_a[A] + c_b[B]) \otimes g(t) \quad \text{(S22)}$$

where $g(t)$ is a Gaussian cross-correlation function for the laser pulses and c_x $(x = a, b)$ is an expansion coefficient. The results are summarized in Table S2. The components of A and B correspond to $^1\pi\pi^*$ and $^1n\pi^*$ signals, respectively. The profiles predominantly reflect the population in the $^1\pi\pi^*$ state, and the $^1n\pi^*$ lifetime is undetermined from this profile. The lifetime of the $^1n\pi^*$ state is discussed later.

Table S2. Best-fit parameters determined by least-squares fitting of the time profile integrated over 3.6-5.2 eV (Thy) and 4.0-5.4 eV (Ura) using Eq. S22.

Parameters	Time constant	Expansion coefficients	
	τ_a	c_a	c_b
Thy	37±1 fs	1.0	0.01
Ura	15±1 fs	1.0	0.003

B. Global fitting analysis

We also performed a global fitting analysis for the results of gaseous sample using Eq. S13. The results are shown in Figures S18 and S19, and the best-fit parameters are summarized in Table S3. The accuracy of the τ_d value is limited because of the measurement time window of 30 ps. The expansion coefficients of c_{xk} $(x = a, b, c, d)$ provide the spectra extracted for each electronic state, as shown in Figures S18(b) and S19(b). From their spectral features, the spectra corresponding to A, (B, C) and D are ascribed to $^1\pi\pi^*$, $^1n\pi^*$ and $^3\pi\pi^*$ states, respectively. The quantum yield for $^1n\pi^*$ was estimated using Eq. S10.

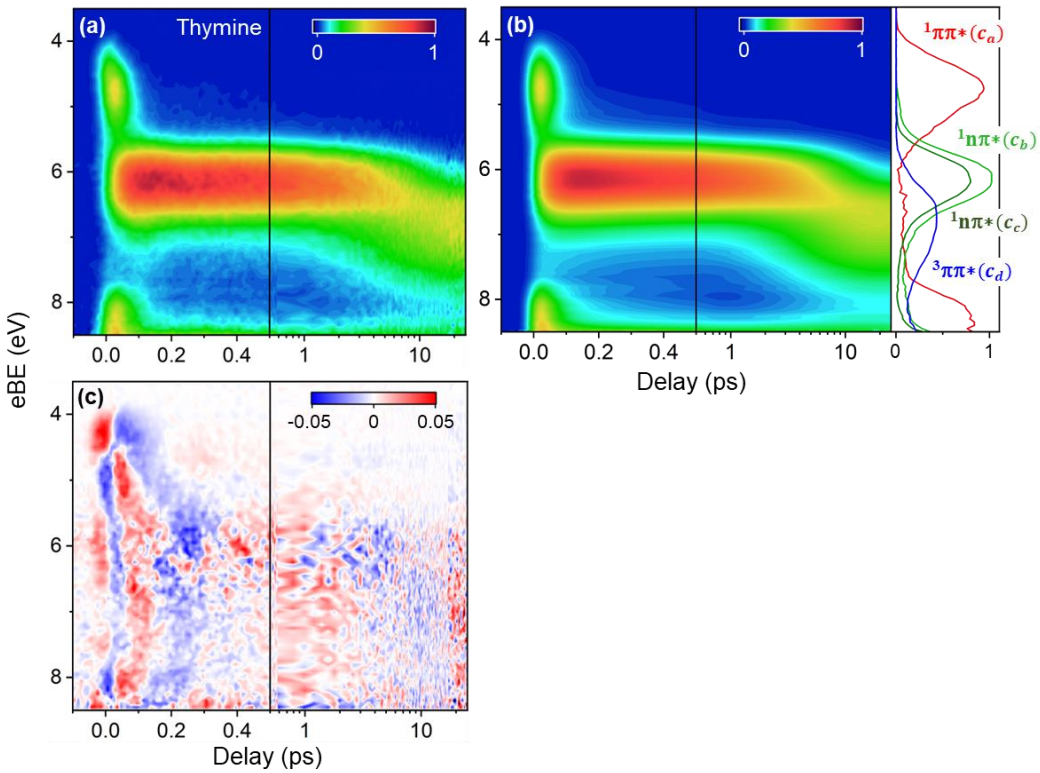

Figure S18. Results of global fitting analysis using EUV-TRPES for gaseous Thy. The horizontal axis is linear up to 0.5 ps and logarithmic thereafter. (a) Experimental two-dimensional map of photoemission spectra. (b) Two-dimensional map of fitted photoemission spectra and extracted spectra for each electronic state using Eq. S13. (c) Difference between (a) and (b).

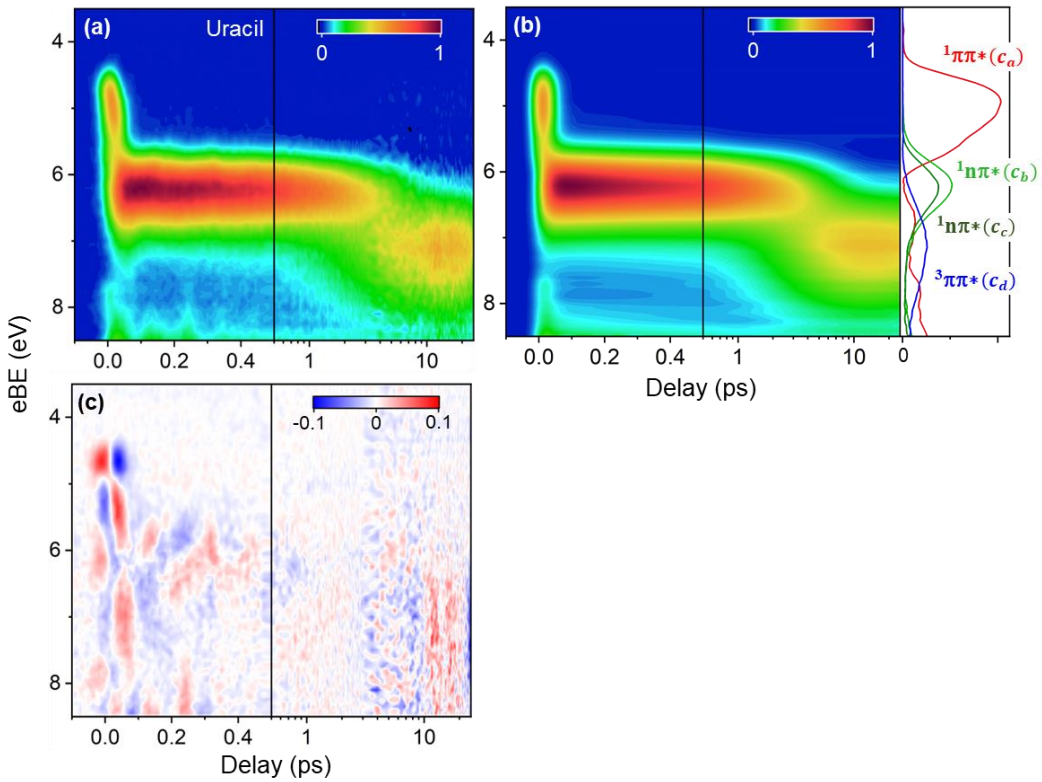

Figure S19. Results of global fitting analysis using EUV-TRPES for gaseous Ura. The horizontal axis is linear up to 0.5 ps and logarithmic thereafter. (a) Experimental two-dimensional map of photoemission spectra. (b) Two-dimensional map of fitted photoemission spectra and extracted spectra for each electronic state using Eq. S13. (c) Difference between (a) and (b).

Table S3. Best-fit parameters in eBE range of 3.5-8.5 eV using Eq. S13.

Parameters	Time constants			
	τ_a	τ_b	τ_c	τ_d
Thy	39±1 fs	0.28±0.01 ps	5.79±0.04 ps	> 30 ps
Ura	17±1 fs	0.44±0.01 ps	3.48±0.03 ps	> 30 ps

Parameters	Areas of the spectrum			
	A	B	C	D
Thy	1.00	1.06	0.74	0.64
(Integration range)	(3.8-6.0 eV)	(5.2-7.2 eV)	(5.2-7.2 eV)	(5.7-8.0 eV)
Ura	1.00	0.45	0.31	0.33
(Integration range)	(4.0-6.2 eV)	(5.3-7.5 eV)	(5.3-7.5 eV)	(5.9-8.2 eV)

C. Comparison with previous studies

Table S4. Excited-state lifetimes (ps) for Thy in gas phase

Pump (nm)	Probe (nm)	τ_1	τ_2	τ_3	Year, Ref
267	800			6.4, >100	2002, 28
250	200	<0.05	0.49	6.4	2004, 29
267	400		0.105	5.12	2005, 30
272	800		0.13	6.5	2005, 31
266	800		0.1	7	2007, 32
267	800		0.1	7, >1000	2008, 33
266	400/800		<0.1	7	2009, 34
266	2.19		0.2-0.3		2014, 35
260	295		0.175	6.13, >1000	2016, 36
267	2.25-2.38	0.06±0.03	1.9±0.1	10.5±0.2	2017, 37
267	88.9	0.08±0.03		3.5±0.3	2019, 38
267	57	0.039±0.001	0.28±0.01	5.79±0.04	2022, This work
Theory					
MRSF-TDDFT		0.03±0.01		6.10±0.04	2021, 39

Table S5. Excited-state lifetimes (ps) for Ura in gas phase

Pump (nm)	Probe (nm)	τ_1	τ_2	τ_3	Year, Ref
267	800			2.4	2002, 28
250	200	<0.05	0.53	2.4	2004, 29
267	400		0.130	1.05	2005, 30
260	295		0.17	2.35, >1000	2016, 36
267	157	0.03			2021, 40
267	57	0.017±0.001	0.44±0.01	3.48±0.03	2022, This work
Theory					
XMS-CASPT2		0.03			2021, 40

References

1. Frassetto, F.; Cacho, C.; Froud, C. A.; Turcu, I. C. E.; Villoresi, P.; Bryan, W. A.; Springate, E.; Poletto, L., Single-Grating Monochromator for Extreme-Ultraviolet Ultrashort Pulses. *Opt. Express* **2011,** *19* (20), 19169-19181.

2. Fuji, T.; Horio, T.; Suzuki, T., Generation of 12 fs Deep-Ultraviolet Pulses by Four-Wave Mixing Through Filamentation in Neon Gas. *Opt. Lett.* **2007,** *32* (17), 2481-2483.

3. Karashima, S.; Humeniuk, A.; Uenishi, R.; Horio, T.; Kanno, M.; Ohta, T.; Nishitani, J.; Mitric, R.; Suzuki, T., Ultrafast Ring-Opening Reaction of 1,3-Cyclohexadiene: Identification of Nonadiabatic Pathway via Doubly Excited State. *J. Am. Chem. Soc.* **2021,** *143* (21), 8034-8045.

4. Kurahashi, N.; Thürmer, S.; Liu, S. Y.; Yamamoto, Y. I.; Karashima, S.; Bhattacharya, A.; Ogi, Y.; Horio, T.; Suzuki, T., Design and Characterization of a Magnetic Bottle Electron Spectrometer for Time-Resolved Extreme UV and X-Ray Photoemission Spectroscopy of Liquid Microjets. *Struct. Dynam.* **2021,** *8* (3), 034303.

5. Ma, C. S.; Cheng, C. C. W.; Chan, C. T. L.; Chan, R. C. T.; Kwok, W. M., Remarkable Effects of Solvent and Substitution on the Photo-Dynamics of Cytosine: a Femtosecond Broadband Time-Resolved Fluorescence and Transient Absorption Study. *Phys. Chem. Chem. Phys.* **2015,** *17* (29), 19045-19057.

6. Buchner, F. Time-Resolved Photoelectron Spectroscopy of DNA Molecules in Solution. Ph. D. Thesis, Free University Berlin, 2015.

7. Martinez-Fernandez, L.; Pepino, A. J.; Segarra-Marti, J.; Jovaisaite, J.; Vaya, I.; Nenov, A.; Markovitsi, D.; Gustavsson, T.; Banyasz, A.; Garavelli, M.; Improta, R., Photophysics of Deoxycytidine and 5-Methyldeoxycytidine in Solution: A Comprehensive Picture by Quantum Mechanical Calculations and Femtosecond Fluorescence Spectroscopy. *J. Am. Chem. Soc.* **2017,** *139* (23), 7780-7791.

8. Hare, P. M.; Crespo-Hernandez, C. E.; Kohler, B., Internal Conversion to the Electronic Ground State Occurs via Two Distinct Pathways for Pyrimidine Bases in Aqueous Solution. *P. Natl. Acad. Sci. U. S. A.* **2007,** *104* (2), 435-440.

9. Xue, B.; Yabushita, A.; Kobayashi, T., Ultrafast Dynamics of Uracil and Thymine Studied Using a Sub-10 fs Deep Ultraviolet Laser. *Phys. Chem. Chem. Phys.* **2016,** *18* (25), 17044-17053.

10. Gustavsson, T.; Banyasz, A.; Lazzarotto, E.; Markovitsi, D.; Scalmani, G.; Frisch, M. J.; Barone, V.; Improta, R., Singlet Excited-State Behavior of Uracil and Thymine in Aqueous Solution: A Combined Experimental and Computational Study of 11 Uracil Derivatives. *J. Am. Chem. Soc.* **2006,** *128* (2), 607-619.

11. Cohen, B.; Crespo-Hernandez, C. E.; Kohler, B., Strickler-Berg Analysis of Excited Singlet State Dynamics in DNA and RNA Nucleosides. *Faraday Discuss.* **2004,** *127*, 137-147.

12. Borrego-Varillas, R.; Nenov, A.; Kabacinski, P.; Conti, I.; Ganzer, L.; Oriana, A.; Jaiswal, V. K.; Delfino, I.; Weingart, O.; Manzoni, C.; Rivalta, I.; Garavelli, M.; Cerullo, G., Tracking Excited State Decay Mechanisms of Pyrimidine Nucleosides in Real Time. *Nat. Commun.* **2021,** *12* (1), 7285.

13. Brister, M. M.; Crespo-Hernandez, C. E., Excited-State Dynamics in the RNA Nucleotide Uridine 5 '-Monophosphate Investigated Using Femtosecond Broadband Transient Absorption Spectroscopy. *J. Phys. Chem. Lett.* **2019,** *10* (9), 2156-2161.

14. Buchner, F.; Nakayama, A.; Yamazaki, S.; Ritze, H. H.; Lübcke, A., Excited-State Relaxation of

Hydrated Thymine and Thymidine Measured by Liquid-Jet Photoelectron Spectroscopy: Experiment and Simulation. *J. Am. Chem. Soc.* **2015,** *137* (8), 2931-2938.

15. Erickson, B. A.; Heim, Z. N.; Pieri, E.; Liu, E.; Martinez, T. J.; Neumark, D. M., Relaxation Dynamics of Hydrated Thymine, Thymidine, and Thymidine Monophosphate Probed by Liquid Jet Time-Resolved Photoelectron Spectroscopy. *J. Phys. Chem. A* **2019,** *123* (50), 10676-10684.

16. Berendsen, H. J. C.; Grigera, J. R.; Straatsma, T. P., The Missing Term in Effective Pair Potentials. *J. Phys. Chem.* **1987,** *91*, 6269.

17. Wang, J.; Wolf, R. m.; Caldwell, J. W.; Kollman, P. A.; Case, D. A., Development and Testing of a General Amber Force Field. *J. Comput. Chem.* **2004,** *25*, 1157.

18. Bayly, C. I.; Cieplak, P.; Cornell, W. D.; Kollman, P. A., A Well-Behaved Electrostatic Potential Based Method Using Charge Restraints for Deriving Atomic Charges: The RESP Model. *J. Phys. Chem.* **1993,** *97*, 10269.

19. Joung, I. S.; Thomas E. Cheatham, I., Determination of Alkali and Halide Monovalent Ion Parameters for Use in Explicitly

Solvated Biomolecular Simulations. *J. Phys. Chem. B* **2008,** *112*, 9020.

20. Martinez, L.; Andrade, R.; Birgin, E. G.; Martinez, J. M., Package for Building Initial Congurations for Molecular Dynamics Simulations. *J. Comput. Chem.* **2009,** *30*, 2157.

21. Allen, M. P.; Tildesley, D. J., *Computer Simulation of Liquids*. Clarendon Press: Oxford, 1987.

22. Hess, B.; Bekker, H.; Berendsen, H. J. C.; Fraaije, J. G. E. M., LINCS: A Linear Constraint Solver for Molecular Simulations. *J. Comput. Chem.* **1997,** *18*, 1463.

23. Nose, S., Unified Formulation of the Constant Temperature Molecular Dynamics Methods. *J. Chem. Phys.* **1984,** *81*, 511.

24. Hoover, W., Canonical Dynamics: Equilibrium Phase-Space Distributions. *Phys. Rev. A* **1985,** *31* (3), 1695-1697.

25. Darden, T.; York, D.; Pedersen, L., Particle Mesh Ewald: An N · log(N) Method for Ewald Sums in Large Systems. *J. Chem. Phys.* **1993,** *98* (12), 10089-10092.

26. Perera, L.; Essmann, U.; Berkowitz, M. L., Effect of the Treatment of Long-Range Forces on the Dynamics of Ions in Aqueous Solutions. *J. Chem. Phys.* **1995,** *102*, 450.

27. Van Der Spoel, D.; Lindahl, E.; Hess, B.; Groenhof, G.; Mark, A. E.; Berendsen, H. J., GROMACS: Fast, Flexible, and Free. *J. Comput. Chem.* **2005,** *26* (16), 1701-18.

28. Kang, H.; Lee, K. T.; Jung, B.; Ko, Y. J.; Kim, S. K., Intrinsic Lifetimes of the Excited State of DNA and RNA Bases. *J. Am. Chem. Soc.* **2002,** *124* (44), 12958-12959.

29. Ullrich, S.; Schultz, T.; Zgierski, M. Z.; Stolow, A., Electronic Relaxation Dynamics in DNA and RNA Bases Studied by Time-Resolved Photoelectron Spectroscopy. *Phys. Chem. Chem. Phys.* **2004,** *6* (10), 2796-2801.

30. Canuel, C.; Mons, M.; Piuzzi, F.; Tardivel, B.; Dimicoli, I.; Elhanine, M., Excited States Dynamics of DNA and RNA Bases: Characterization of a Stepwise Deactivation Pathway in the Gas Phase. *J. Chem. Phys.* **2005,** *122* (7).

31. Samoylova, E.; Lippert, H.; Ullrich, S.; Hertel, I. V.; Radloff, W.; Schultz, T., Dynamics of Photoinduced Processes in Adenine and Thymine Base Pairs. *J. Am. Chem. Soc.* **2005,** *127* (6), 1782-1786.

32. Gador, N.; Samoylova, E.; Smith, V. R.; Stolow, A.; Rayner, D. M.; Radloff, W. G.; Hertel, I. V.; Schultz, T., Electronic Structure of Adenine and Thymine Base Pairs Studied by Femtosecond Electron-Ion Coincidence Spectroscopy. *J. Phys. Chem. A* **2007,** *111* (46), 11743-11749.

33. Samoylova, E.; Schultz, T.; Hertel, I. V.; Radloff, W., Analysis of Ultrafast Relaxation in Photoexcited DNA Base Pairs of Adenine and Thymine. *Chem. Phys.* **2008,** *347* (1-3), 376-382.

34. Gonzalez-Vazquez, J.; Gonzalez, L.; Samoylova, E.; Schultz, T., Thymine Relaxation after UV Irradiation: the Role of Tautomerization and πσ* States. *Phys. Chem. Chem. Phys.* **2009,** *11* (20), 3927-3934.

35. McFarland, B. K.; Farrell, J. P.; Miyabe, S.; Tarantelli, F.; Aguilar, A.; Berrah, N.; Bostedt, C.; Bozek, J. D.; Bucksbaum, P. H.; Castagna, J. C.; Coffee, R. N.; Cryan, J. P.; Fang, L.; Feifel, R.; Gaffney, K. J.; Glownia, J. M.; Martinez, T. J.; Mucke, M.; Murphy, B.; Natan, A.; Osipov, T.; Petrovic, V. S.; Schorb, S.; Schultz, T.; Spector, L. S.; Swiggers, M.; Tenney, I.; Wang, S.; White, J. L.; White, W.; Guhr, M., Ultrafast X-Ray Auger Probing of Photoexcited Molecular Dynamics. *Nat. Commun.* **2014,** *5*.

36. Yu, H.; Sanchez-Rodriguez, J. A.; Pollum, M.; Crespo-Hernandez, C. E.; Mai, S.; Marquetand, P.; Gonzalez, L.; Ullrich, S., Internal Conversion and Intersystem Crossing Pathways in UV Excited, Isolated Uracils and Their Implications in Prebiotic Chemistry. *Phys. Chem. Chem. Phys.* **2016,** *18* (30), 20168-20176.

37. Wolf, T. J. A.; Myhre, R. H.; Cryan, J. P.; Coriani, S.; Squibb, R. J.; Battistoni, A.; Berrah, N.; Bostedt, C.; Bucksbaum, P.; Coslovich, G.; Feifel, R.; Gaffney, K. J.; Grilj, J.; Martinez, T. J.; Miyabe, S.; Moeller, S. P.; Mucke, M.; Natan, A.; Obaid, R.; Osipov, T.; Plekan, O.; Wang, S.; Koch, H.; Guhr, M., Probing Ultrafast ππ*/nπ* Internal Conversion in Organic Chromophores via K-Edge Resonant Absorption. *Nat. Commum.* **2017,** *8*.

38. Wolf, T. J. A.; Parrish, R. M.; Myhre, R. H.; Martinez, T. J.; Koch, H.; Guhr, M., Observation of Ultrafast Intersystem Crossing in Thymine by Extreme Ultraviolet Time-Resolved Photoelectron Spectroscopy. *J. Phys. Chem. A* **2019,** *123* (32), 6897-6903.

39. Park, W.; Lee, S.; Huix-Rotllant, M.; Filatov, M.; Choi, C. H., Impact of the Dynamic Electron Correlation on the Unusually Long Excited-State Lifetime of Thymine. *J. Phys. Chem. Lett.* **2021,** *12* (18), 4339-4346.

40. Chakraborty, P.; Liu, Y. S.; McClung, S.; Weinacht, T.; Matsika, S., Time Resolved Photoelectron Spectroscopy as a Test of Electronic Structure and Nonadiabatic Dynamics. *J. Phys. Chem. Lett.* **2021,** *12* (21), 5099-5104.